European Journal of Medicinal Chemistry 297 (2025) 117926

Contents lists available at ScienceDirect

European Journal of Medicinal Chemistry

journal homepage: www.elsevier.com/locate/ejmech

Research paper

Mitochondrial-targeted iridium(III) complexes suppress tumor growth through inducting immunogenic cell death to activate immune response

Shuanghui Tang [a], Yueyao Ding [b], Ziyan Zhang [b], Yan Yang [c,*], Chunxia Huang [a], Lin Zhou [a], Shuang Tian [a], Hui Yin [b,**], Yunjun Liu [a,***]

[a] School of Pharmacy, Guangdong Pharmaceutical University, Guangzhou, 510006, PR China
[b] Department of Microbiology and Immunology, Guangdong Pharmaceutical University, Guangzhou, 510006, PR China
[c] Department of Pharmacy, The Affiliated Guangdong Second Provincial General Hospital of Jinan University, Guangzhou, 510317, PR China

ARTICLE INFO

Keywords:
Iridium(III) complexes
Mitochondrial targeting
Ferroptosis
Antitumor in vivo
Immune response

ABSTRACT

A new ligand, 2-(2-hydroxyl-4-methyl)phenyl-1H-imidazo[4,5-f][1,10]phenanthroline (IPMP), and [Ir(ppy)$_2$(IPMP)]PF$_6$ (7a), [Ir(bzq)$_2$(IPMP)]PF$_6$ (7b), and [Ir(piq)$_2$(IPMP)]PF$_6$ (7c) have been prepared and characterized by HRMS, NMR spectra. The 3-(4,5-dimethylthiazol-2-yl)-2,5-diphenyltetrazolium bromide (MTT) assays revealed that 7b exhibited excellent activity (IC$_{50}$ = 4.5 ± 0.4 μM), while 7a and 7c showed good cytotoxicity (IC$_{50}$ = 8.5 ± 0.9 μM and 8.9 ± 2.2 μM) against non-small cell lung cancer A549 cells. The experiments of cellular uptake and mitochondrial localization demonstrate that these new iridium(III) complexes are readily taken up by A549 cells and accumulate in the mitochondria and damage the structure of the mitochondria, which results in the loss of mitochondrial membrane potential (MMP), elevated lipid peroxidation, as well as DNA damage, the inhibition of microtubule polymerization, hindrance of the cell cycle in the G0/G1 phase, and release of cytochrome *c*, collectively leading to apoptosis. Furthermore, upregulation of Beclin-1, overexpression of NF-κB and downregulation of GPX4 protein were observed, which resulted in the activation of autophagy, pyroptosis and ferroptosis, respectively. In the C57BL/6 mouse model, the 7b demonstrated promising in vivo antitumor efficacy, with a tumor inhibitory rate of 66.9 %. Additionally, the complexes induce an immunogenic cell death to activate immune response, further enhance CD8$^+$ T cells and efficiently inhibit tumor growth. Collectively, we consider that the complexes may be utilized as potential candidate agents for the treatment of A549 cancer.

1. Introduction

Cancers are prevalent and pose a serious threat to human health. Lung cancer has one of the highest incidence rates of any malignancy worldwide, exceeding those of breast, prostate, and colorectal cancers. Furthermore, it is the leading cause of cancer-related mortality [1]. Lung cancer can be classified into two primary categories: small cell lung cancer (SCLC) and non-small cell lung cancer (NSCLC). NSCLC constitutes the majority (up to 85 % of total cases) and exhibits a 5-year survival rate of just 15.9 % [2]. At present, chemotherapy is one of the most widely used and effective strategies for NSCLC treatment compared to other approaches, such as surgery, molecularly targeted therapies, and immunotherapies [3–7].

Anticancer chemotherapeutic agents based on platinum (Pt) such as cisplatin (approval by the FDA in 1978) are widely used, but their severe side effects and resistance have limited their clinical application [8–11]. Therefore, there is a critical need for the development of a broad-spectrum, high-potency, and low-toxicity metal-based anticancer drug. Recently, the coordination of iridium(III) has emerged as a promising approach in the design of antitumor drugs [12]. In comparison to the planar Pt(II) complexes, the unique structural multiplicity and versatility conferred by the octahedral coordination of Ir(III) have been shown to enhance the feasibility of biomolecular targeting. In addition, Ir(III) complexes possess luminescent imaging and therapeutic functions that will be beneficial for the visualization of anti-cancer mechanisms [13,14]. Some Ir(III) complexes have been found to exhibit high

---

* Corresponding author.
** Corresponding author.
*** Corresponding author.
E-mail addresses: yany@gd2h.org.cn (Y. Yang), huiyin0103@gdpu.edu.cn (H. Yin), lyjche@gdpu.edu.cn (Y. Liu).

https://doi.org/10.1016/j.ejmech.2025.117926
Received 16 April 2025; Received in revised form 29 June 2025; Accepted 30 June 2025

selectivity for various cancer cell lines and effectively to target mitochondria [15–17], leading to mitochondrial dysfunction and the inhibition of cancer cell proliferation. In recent years, researchers discovered that a lot of metal complexes including Ir(III), Cu(I), Rh(III), Ru(II) show excellent anticancer efficiency [18–26]. Liang et al. reported that iridium(III) complexes accumulated the mitochondrial inner membrane of HeLa cells with high selectivity and exhibited a high antineoplastic activity [27]. Ortyl reported that iridium(III) complexes can produce ROS upon light activation and act as photosensitizers for photodynamic therapy (PDT) to cause cell death [28]. In addition, activation of immune response to increase CD8$^+$ T cells has been paid a great attention, Liu et al. found that a Ru(II) complex causes an immunogenic cell death, which activated an immune response to enhance CD8$^+$ T cells, further induced an increment of TNF-α, IFN-γ and a decrease of IL-10 amount and efficiently prevent tumor growth [29]. Yang et al. reported that an Ir(III) complex directly kill liver cancer cells through inducing necroptosis and activating the necroptosis-related immune response [30]. Liang et al. found that the Ru(III) complexes trigger Gasdermin E-mediated pyroptosis and an immune response to induce cell death [31]. To obtain more information on anticancer activity and mechanism of Ir(III) complexes, we prepared a new ligand 2-(2-hydroxyl-4-methyl)phenyl-1H-imidazo[4,5-f][1,10] phenanthroline (IPMP) and its three Ir(III) complexes: [Ir(ppy)$_2$(IPMP)]PF$_6$ (7a), [Ir(bzq)$_2$(IPMP)]PF$_6$ (7b), and [Ir(piq)$_2$(IPMP)]PF$_6$ (7c) (Scheme 1). The cytotoxicity of 7a, 7b and 7c against cancerous (A549, LA795) and normal (NIH3T3) cells was evaluated using the 3-(4, 5-dimethylthiazole)-2,5-diphenyltetrazolium bromide (MTT) assay. The cellular apoptosis, cell substructure localization and antitumor molecular mechanisms of 7a, 7b and 7c on A549 cells were investigated in detail. Finally, the antitumor in vivo efficacy of 7b was evaluated in the subcutaneous A549 tumor-bearing nude mouse model and the antitumor mechanism was explored.

2. Results and discussion

2.1. Synthesis and characterization of 7a, 7b and 7c

IPMP was obtained by refluxing 1,10-phenanthroline-5,6-dione, NH_4Ac and 2-hydroxyl-4-methylbenzaldehyde in glacial acetic acid. 7a, 7b and 7c were gained by the reaction of IPMP with [Ir(ppy)$_2$Cl]$_2$·H$_2$O, [Ir(bzq)$_2$Cl]$_2$·H$_2$O, or [Ir(piq)$_2$Cl]$_2$·H$_2$O in a mixed solvent of methanol and dichloromethane. These compounds were purified through the neutral column chromatography to gain the desired 7a, 7b and 7c. These complexes were characterized by HRMS, NMR. The

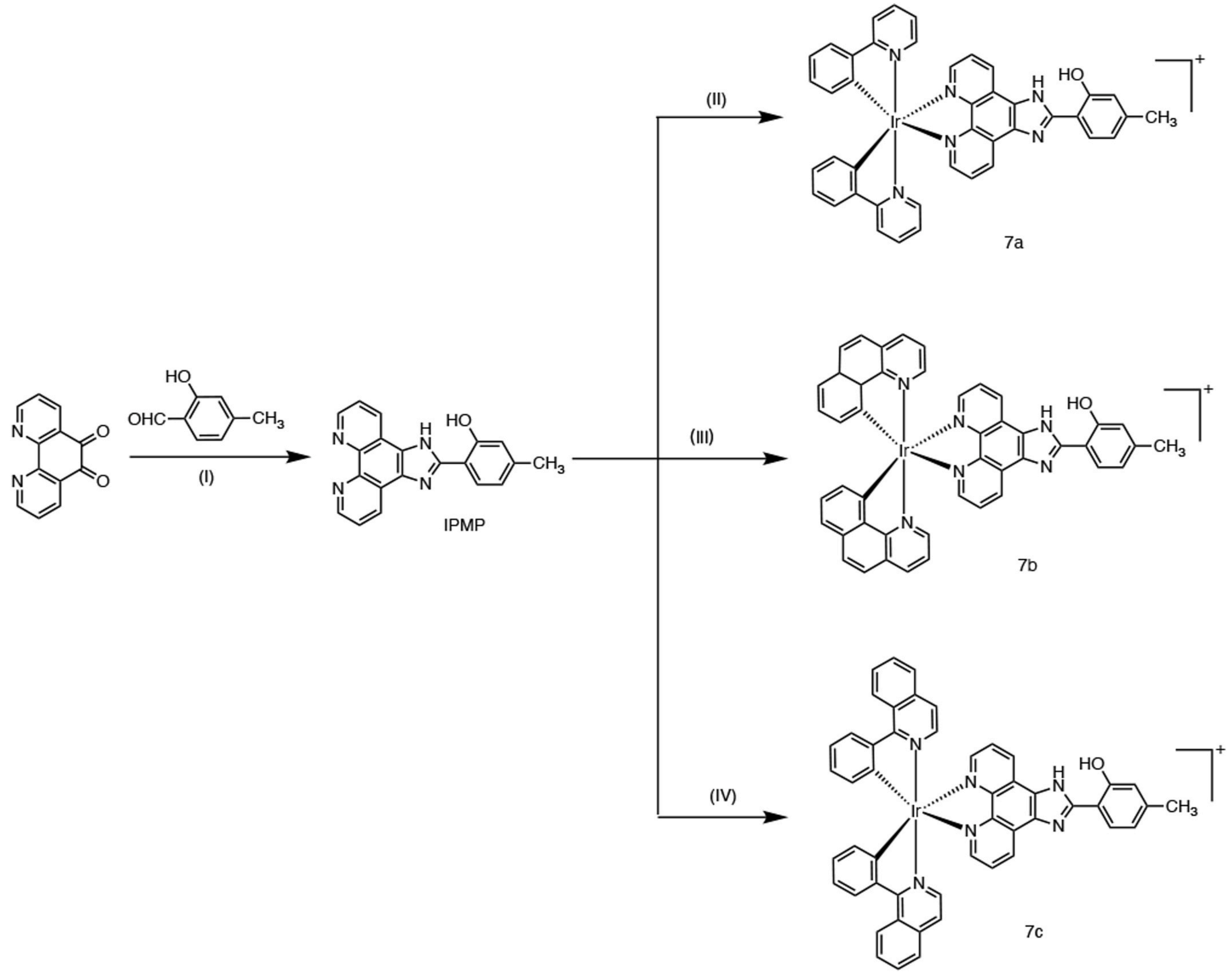

Scheme 1. Synthetic route for ligand IPMP and complexes 7a, 7b, 7c.

Synthetic conditions, reagents, and solvent: (I) NH_4Ac, HAc, reflux for 2 h at 130 °C; (II) [Ir(ppy)$_2$Cl]$_2$, 15 mL CH_3OH, 30 mL CH_2Cl_2, reflux for 6 h at 40 °C under Ar; (III) [Ir(bzq)$_2$Cl]$_2$, 15 mL CH_3OH, 30 mL CH_2Cl_2, reflux for 6 h at 40 °C under Ar; (IV) [Ir(piq)$_2$Cl]$_2$, 15 mL CH_3OH, 30 mL CH_2Cl_2, reflux for 6 h at 40 °C under Ar.

results from HRMS show that the calculated values are consistent with the determined molecular weights. ^{1}H NMR spectra show that the peaks of 2.33, 2.35, 2.30 and 2.31 ppm for IPMP, 7a, 7b and 7c are assigned to the proton of $-CH_3$. The signal of the proton of the hydroxyl group (-OH) in the benzene ring was not found. Likely due to a rapid interchange between the two nitrogen atoms within the imidazole ring, the signal of the proton in the imidazole ring was not also observed. In the ^{13}C NMR spectra, the signals of 21.60, 21.66, 21.53 and 21.62 ppm for IPMP, 7a, 7b and 7c are attributed to the $-CH_3$.

To investigate the stability of 7a, 7b and 7c in PBS solution, the UV–Vis absorption spectra of 7a, 7b and 7c at 0 h and 24 h were recorded. As illustrated in Fig. S1a (SI), the complexes (20 μM) exhibited an absorption at wavelengths of 256 nm ($\varepsilon = 24300$) for 7a, 250 nm ($\varepsilon = 26500$) and 345 nm ($\varepsilon = 17400$) for 7b, 297 nm ($\varepsilon = 14050$) and 362 nm ($\varepsilon = 12900$) for 7c. At room temperature, in PBS solution, the peak shape at 0 h and 24 h remained unchanged, indicating that these complexes are stable. Additionally, we used fluorescence spectra to examine the stability of the complexes in PBS solution at 0 and 24 h, see from Fig. S1b (SI), no change in the peak shape also indicates that the complexes are stable in PBS solution.

Using methanol and water as mobile phase, the purity of 7a, 7b and 7c was examined by HPLC (Lc25, C18 column, flow rate 3 mL/min, Rehen Technology, China). A main peak was uncovered, showing that 7a, 7b, 7c are pure (>95 %) (Fig. S2 and SI).

2.2. *In vitro cytotoxic activity, cell colony and wound healing studies*

The complexes were dissolved in DMSO and diluted with PBS to obtain different concentration of 7a, 7b and 7c. To evaluate the anticancer activity of these complexes in vitro, the antiproliferative activities of 7a, 7b and 7c toward A549, LA795 and normal cell NIH3T3 were investigated by the 3-(4,5-dimethylthiazol-2-yl)-2,5-diphenyltetrazolium bromide (MTT) method [32]. The IC_{50} values for 7a, 7b and 7c are presented in Table 1. In detail, all the complexes exhibit excellent toxicity against the A549 cells with IC_{50} values of 8.5 ± 0.9 μM for 7a, 4.5 ± 0.4 μM for 7b, and 8.9 ± 2.2 μM for 7c. 7b shows higher anticancer activity than cisplatin on A549 and LA795 cells, their cytotoxic activity is comparable to that of liposome-entrapped complex $[Ir(ppy)_2(BAPIP)](PF_6)$ ($IC_{50} = 4.9 \pm 1.0$ μM) [18]. We also discovered that the complexes reveal moderate cytotoxic activity on normal NIH3T3 cells. Additionally, we also determined the IC_{50} value of ligand IPMP against A549 cells, we found that IPMP shows moderate cytotoxic activity toward A549 cells, furthermore, the cytotoxic activity enhances after the ligand was formed complexes. The anticancer efficiency follows the order of 7b > 7a > 7c on A549 and LA795 cells. This can be explained by the energy gap (ΔE) between the lowest unoccupied orbital (LUMO) and the highest occupied orbital (HOMO). Geometry optimization of compounds 7a-7c with orbital calculations was performed using Gaussian 09 package [33] at the level of B3LYP density functional in conjunction with the 6-31G(d) basis sets for C, H, N, O atoms, LanL2DZ for Ir atom. Generally, the small ΔE value leads to high anticancer efficiency. As depicted in Fig. 1 and Table 1, the electronic clouds mainly focus on phenanthroline in the LUMO orbitals, whereas the electronic clouds in HOMO orbitals mainly focus on the ancillary ligands ppy, bzq and piq. The ΔE values of $E_{LUMO} - E_{HOMO}$ or $E_{S1} - E_{T1}$ follow the order of 7b < 7a < 7c, which aligns with those of cytotoxicity of 7b > 7a > 7c. Similar results can be found in other iridium(III) complexes [19,34]. Due to these complexes exhibiting high cytotoxic activity towards A549 cells, this cell line was selected for the subsequent experiments.

Inhibition of tumor proliferation and metastasis represents a crucial aspect of cancer treatment [35]. To investigate the inhibitory effects of 7a, 7b and 7c on the proliferative and migratory abilities of A549 cells, cell colony and wound healing assays were performed. As shown in Fig. S3a (SI), the number of A549 cell in 7a, 7b and 7c-treated groups significantly reduced compared with that in the control, indicating that these Ir-complexes effectively inhibit the cell colony. Additionally, A549 cells were co-cultured with IC_{50} concentration of 7a, 7b and 7c for 24 h to assess the efficacy of these compounds on inhibiting wound healing. Fig. S3b (SI) showed that 7a, 7b and 7c can significantly suppress the cell migration. The scratch condition was quantitatively analyzed using Image J software, as shown in Fig. S3c (SI), compared to the control group with a healing degree of 0.50, the healing degrees in the 7a, 7b and 7c scratches are 0.27, 0.32 and 0.28, respectively, which further suggests that 7a, 7b and 7c can effectively block cell migration. Additionally, FAK (focal adhesion kinase) protein assumes a pivotal role, which can control the adhesion, migration, invasion, and proliferation of cells. Its overexpression in a wide variety of cancers can lead to a poor cancer prognosis [36]. As illustrated in Fig. S3d (SI), the expression of intracellular FAK protein was found to be decreased after 20 h of exposure to 7a, 7b and 7c, providing substantial evidence that 7a, 7b and 7c are capable of inhibiting the migration and proliferation in A549 cells.

Angiogenesis is an important pathological feature of tumorigenesis, and inhibition of angiogenesis is an effectively method for tumor therapy. As depicted in Fig. S3e (I) (SI), we found a reduction of the number of tumor vasculature after a 6 h treatment of A549 cells with 4.5 μM of 7b, indicating that 7b can prevent the angiogenesis. In addition, VEGFA (vascular endothelial growth factor A) is a highly specific pro-vascular endothelial growth factor, which promotes increasing vascular permeability, extracellular matrix degeneration, vascular endothelial cell migration, proliferation, and angiogenesis, hence, inhibition of the expression of VEGFA is an important manner to prevent the tumor cell proliferation, observing from Fig. S3e (II) (SI), 7a-7c can inhibit the expression of VEGFA, which shows that 7a, 7b and 7c block the tumor angiogenesis, further prevent the cancer proliferation. Taken together, the complexes can efficiently block cell proliferation and migration.

2.3. *Cellular uptake, co-localization, change of mitochondrial membrane, release of cytochrome c and apoptosis*

The initial step in the anti-cancer effect of a drug is its capability of crossing the cellular membrane. Thus, the cellular uptake was explored. As illustrated in Fig. S4 (SI), while a 12 h of co-incubation of A549 cells with 8.5 μM of 7a, 4.5 μM of 7b and 8.9 μM of 7c, we found that Hoechst 33342 stained the cell nuclei blue, 7a, 7b, and 7c emitted green fluorescence. The envelopment of the blue by the green indicated that 7a, 7b, and 7c are able to enter the cancer cell to cumulate in the cytoplasm.

Mitochondria represent a pivotal cellular organelle in eukaryotic cells, with a pivotal role in both the induction and control of apoptosis. The mitochondria-specific red fluorescently labeled probe

Table 1

IC_{50} values (μM) of IPMP, 7a, 7b, 7c toward cancer cells for 48 h and the energy of LUMO, HOMO, S1, T1 (eV).

complex	A549	LA795	NIH3T3	LUMO	HOMO	ΔE_{L-H}	S1	T1	ΔE_{S1-T1}
IPMP	11.8 ± 2.1	–	–						
7a	8.5 ± 0.9	13.1 ± 3.0	12.5 ± 2.3	−4.6055	−7.5383	2.9328	2.5506	1.8953	0.6553
7b	4.5 ± 0.4	8.3 ± 0.3	12.0 ± 0.5	−4.5818	−7.4268	2.8450	2.5315	1.9157	0.6159
7c	8.9 ± 2.2	43.2 ± 2.2	14.7 ± 2.7	−4.4806	−7.4319	2.9513	2.4328	1.4079	1.0249
cisplatin	6.6 ± 0.7	19.0 ± 0.5	18.3 ± 2.4						

Data for cisplatin from Ref [23,37].

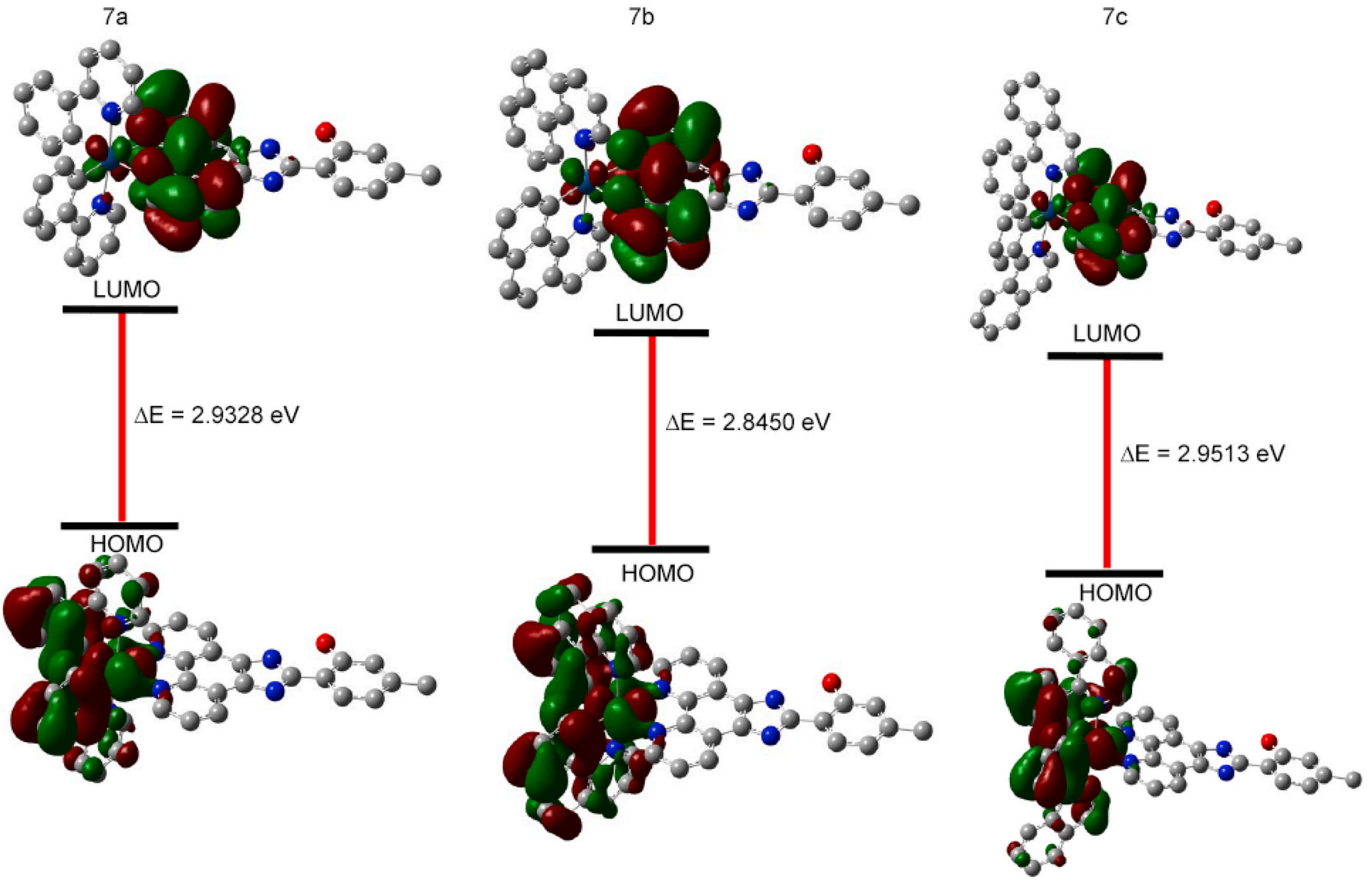

Fig. 1. The energy gap between LUMO and HOMO (eV) of 7a, 7b and 7c.

MitoTracker® Deep Red FM (ThermoFisher, 100 nM) was employed to investigate the co-localization of 7a, 7b and 7c in the mitochondria. Fig. S5a (SI) depicts in the control condition, wherein mitochondria were stained red. Following a 4 h treatment period, the merge (yellow) of red and green fluorescence (emitted by the complexes) suggests that 7a, 7b, 7c locate at the mitochondria. In our recent work, we found that the complexes enter the cancer cells to accumulate in the cytoplasm, and finally the complexes focus on the mitochondria, Consequently, the accumulation of the complexes in the organelles is a dynamical process [29]. The ICP-MS experiments have been performed and we found that the amounts of 7b distributing in the mitochondria and cell nuclei are 10.3030 (±1.04) and 0.7284 (±0.11) ng/10^6 cells after a treatment of 24 h of A549 cells with 10 μM of 7b, hence, most of the complex distributes at the mitochondria.

Afterwards, we examined the impact of the complex on the mitochondrial structure through transmission electron microscopy (TEM). As seen from Fig. 2a, we observed the changes in the mitochondrial morphology in A549 cells. In the blank group, the mitochondrial morphology was well preserved, the inner and outer membranes were intact, and the cristae were obvious. In contrast, the mitochondrial structure in the 7c-treated group was significantly altered. Vacuolar structures were formed in the mitochondrial matrix, and cristae were irregularly structured and appeared to be broken or fused, indicating loss of contents and almost complete impairment of function.

A normal mitochondrial membrane potential is important for safeguard of the functions of mitochondrial oxidative phosphorylation and adenosine 5′-triphosphate (ATP) production. The impairment of mitochondrial function is manifested by increased mitochondrial membrane permeability, decreased membrane potential, the release of cytochrome *c* (cyto c), and ultimately apoptosis [38]. To further evaluate the impact of 7a, 7b and 7c on the changes in the mitochondrial membrane potential (MMP), JC-1 (5,5′,6,6′-tetrachloro-1,1′,3,3′-tetraethyl-imidacarbocyanine), a fluorescent probe, was utilized. JC-1 is a specific marker of membrane potential, as aggregates JC-1 emits red fluorescence, which is because the cell membrane potential is at a high potential, and damaged cells by depolarizing MMP, as monomer JC-1 is broken down (green). As Seen from Fig. S5b (SI), the control group exhibits intense red fluorescence, whereas A549 cells exhibit a notable green fluorescence after 20 h of treatment with the IC_{50} concentration of 7a, 7b and 7c. The results indicate that the MMP decreased following a treatment of A549 cells with 7a, 7b and 7c. The use of a cyto c antibody in conjunction with specific immunolabeling revealed that A549 cells co-incubated with 7a, 7b and 7c for 20 h exhibited a more pronounced green fluorescence in comparison to the control group (Fig. S5c and SI). This indicates that the cells can release a significant amount of cyto c molecules from their mitochondria.

7a, 7b and 7c co-localized at the mitochondria, disrupt the mitochondrial structure and function and induce a release of cyto c from the mitochondria, which can activate caspase 3, finally cause cell apoptosis. To ascertain the impact of 7a, 7b, and 7c on apoptosis in A549 cells, the apoptotic percentage was examined. As illustrated in Fig. 2b, the control group (I) exhibited an early and late apoptotic percentage of 5.92 %. Following the treatment of A549 cells with 7a (II), 7b (III), and 7c (IV) over a period of 20 h, the early and late apoptotic percentage of A549 cells was found to be 40.1 %, 43.21 % and 45.1 %, respectively, the apoptotic percentage increases by 34.18 % for 7a, 37.29 % for 7b and 39.18 % for 7c. These results clearly show that 7a, 7b and 7c can efficiently cause apoptosis.

The mitochondrial damage-mediated intrinsic pathway has been demonstrated to induce apoptosis in A549 cells [39,40]. A series of proteins associated with the intrinsic pathway to induce apoptosis was examined for the expression levels by western blotting. On the one hand,

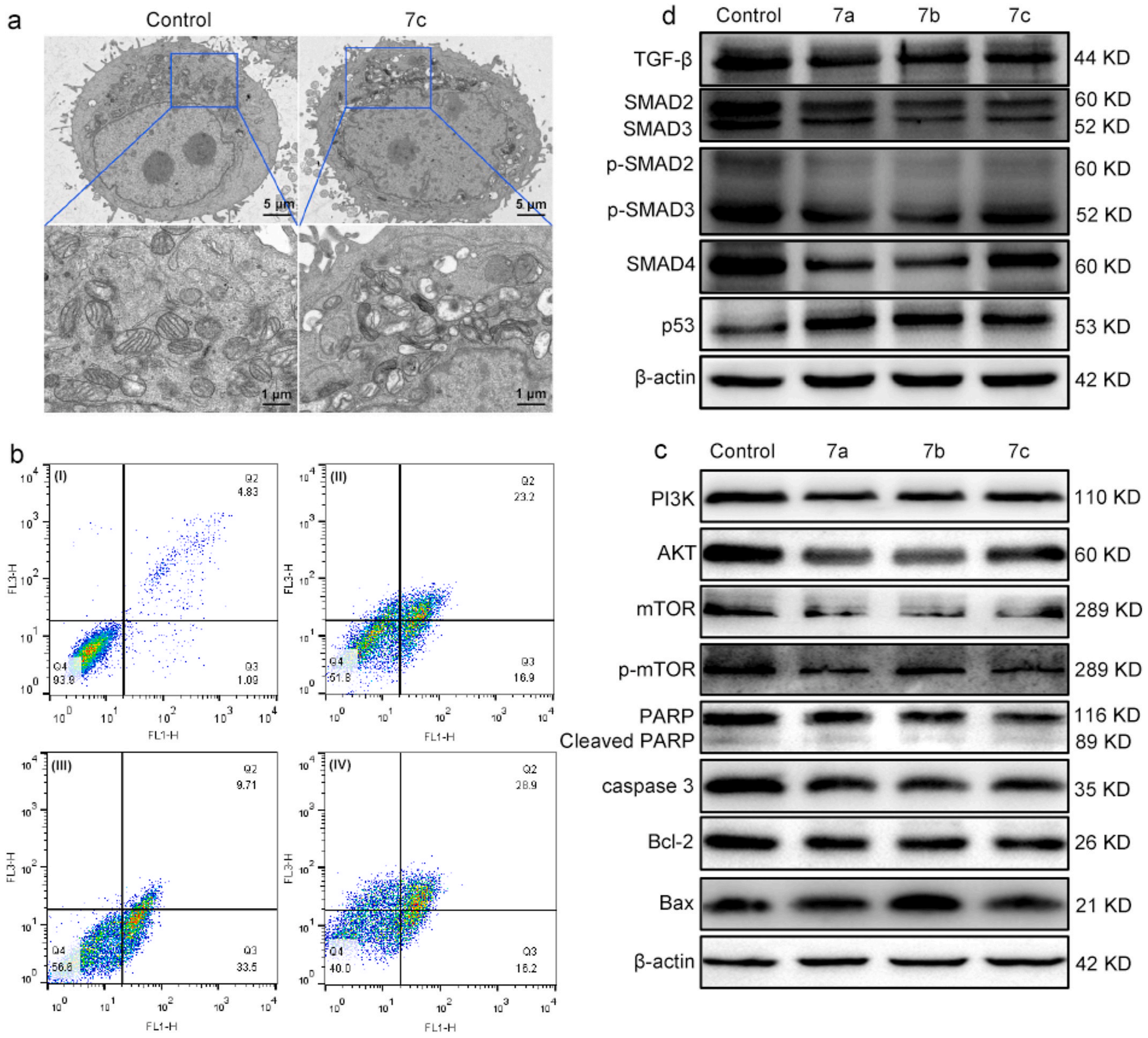

Fig. 2. (a) Mitochondrial structure damage while A549 cells were treated with 2 × IC_{50} concentration of 7c for 24 h, (b) apoptotic percentage after the treatment of A549 cells (I) with IC_{50} concentration of 7a (II), 7b (III) and 7c (IV) for 20 h, (c) expression of PARP, caspase 3, Bcl-2, Bax, PI3K, AKT, mTOR and p-mTOR proteins, (d) TGF-β and p53 signaling pathways while A549 cells were treated with IC_{50} concentration of 7a, 7b and 7c for 24 h.

protein molecules containing the BH_3 structure play a pivotal role in regulating the intrinsic pathway, including BID, Bax, and Bcl-2 [41,42]. On the other hand, the initiation of apoptosis results in the degradation of caspase 3, an apoptotic execution factor, which is employed to cleave the cellular substrate poly ADP-ribose polymerase (PARP) [43,44]. As shown in Fig. 2c, a reduction in the expression level of caspase 3 was observed following the co-incubation of A549 cells with 7a, 7b and 7c for 24 h, indicating that caspase 3 was activated. Additionally, the expression level of PARP was downregulated and cleavage occurs, indicating that PARP was cleaved and activated by caspase 3. At the same time, it was also observed that the expression of the anti-apoptotic Bcl-2 was downregulated, while the expression of pro-apoptotic Bax was upregulated. The results demonstrated that 7a, 7b, and 7c induced apoptosis through the intrinsic pathway, which is mediated by mitochondrial damage. Additionally, 7a, 7b and 7c inhibit PI3K, AKT, mTOR and p-mTOR. Therefore, 7a-7c also trigger apoptosis through blocking PI3K/AKT/mTOR signaling pathway.

In addition, we explored the TGF-β and p53 signaling pathways. As depicted in Fig. 2d, the complexes downregulated the expression of TGF-β, activated SMAD pathway, downregulated the expression of SMAD2, SMAD3, p-SMAD2, p-SMAD3 and SMAD4, we also discovered that the complexes increased the expression of p53 protein. Taken together, the complexes cause cell death through TGF-β/SMAD and p53 signaling pathways.

2.4. *DNA damage, tubulin polymerization, cell cycle arrest and autophagy*

DNA damage can impede DNA replication and induce cell cycle arrest through discrete mechanisms. When a double-strand DNA break occurs, the core histones H_2AX is phosphorylated to generate γH_2AX, which is an important marker for detecting the DNA damage [45,46]. As illustrated in Fig. 3a, the control group displays a weak green fluorescence, while the cells treated with 7a, 7b, and 7c exhibit distinct green fluorescence following co-incubation with the γH_2AX antibody. Consequently, it can be surmised that 7a, 7b, and 7c can induce DNA double-strand breaks.

The processes of replication and division that occur during the cell cycle are accompanied by significant alterations to the cytoskeleton and cell morphology [47,48]. Microtubule structures play an important role in numerous biological processes. They are essential for transport of substances and the transduction of signals, and they also maintain the morphological structure of cells [49]. Mutations and mis-regulation of microtubule structure result in errors in cell cycle division, which in turn leads to cell cycle arrest. The microtubule morphology remained unaltered in the control cells, exhibiting a perfectly ordered and tightly packed structure. However, following the administration of 7a, 7b and 7c for a period of 20 h, the cell microtubule structure exhibited a

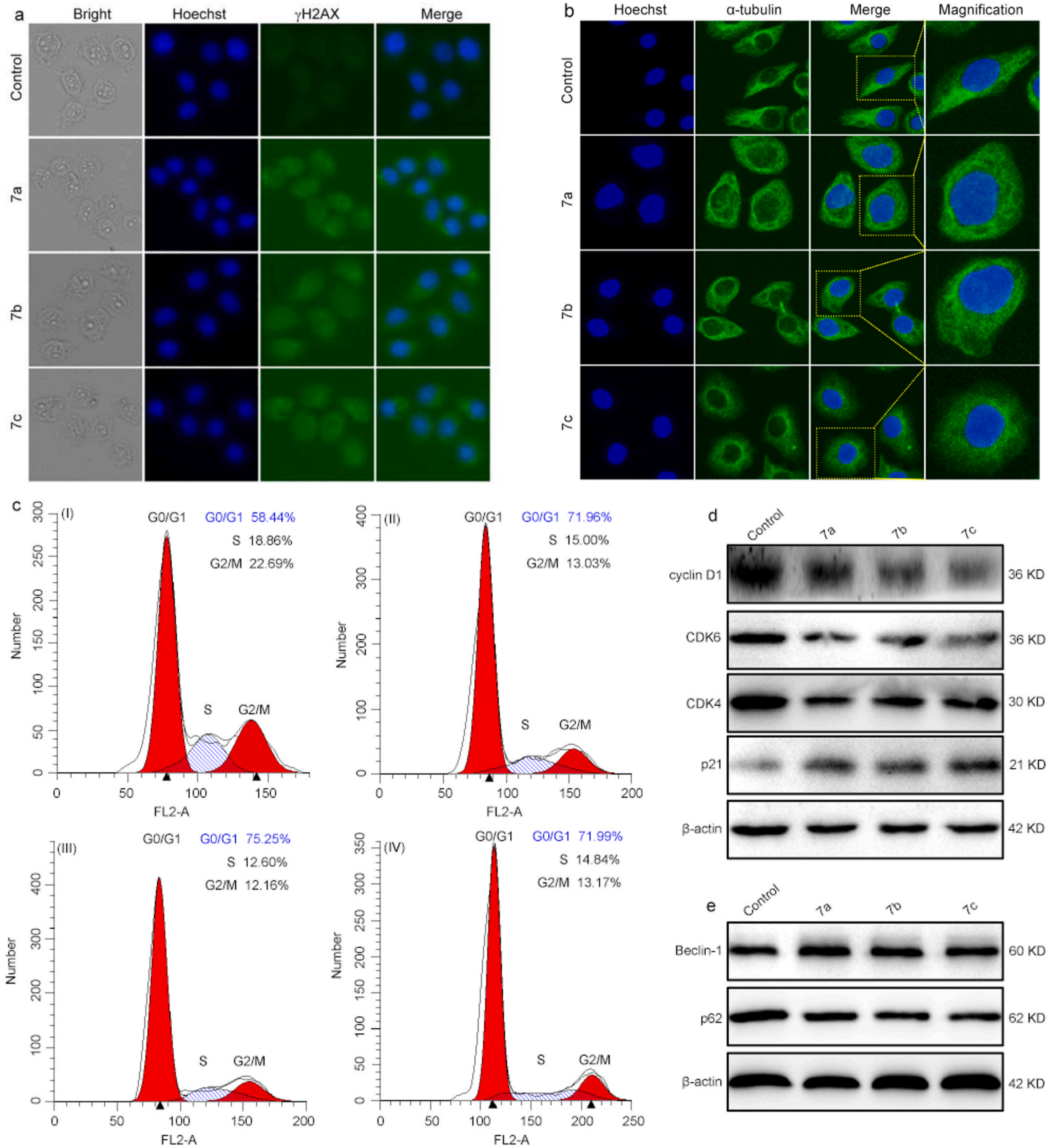

Fig. 3. (a) DNA-damage via determination of γ-H2AX, (b) The α-tubulin measurement, (c) cell cycle distribution, control (I), 7a (II), 7b (III), 7c (IV), (d) expression of cell cycle-related proteins, (e) autophagy, while A549 cells were incubated with IC_{50} concentration of 7a, 7b and 7c for 20 h.

dispersed configuration (Fig. 3b). The results demonstrate that 7a, 7b and 7c are capable of impeding cell cycle progression and inducing cell death by disrupting the normal microtubule structure of cells.

To elucidate the mechanism of 7a, 7b and 7c inhibiting cell proliferation, an assay of the cell cycle arrest was performed. As seen from Fig. 3c, we uncovered a large increase of 13.52 % for 7a (II), 16.81 % for 7b (III), and 13.55 % for 7c (IV) in the G0/G1 phase in comparison to the control, meanwhile, we also observed a reduction in the S and G2/M phases. These results indicate that 7a, 7b and 7c block cell proliferation during the G0/G1 phase.

Cell cycle assays have demonstrated that 7a, 7b and 7c induce A549 cell cycle arrest in G0/G1 phases. Additionally, it has been established that the progression of G1 phases cells necessitates integrin-dependent signaling, particularly cyclin D1 induction and positive regulation of cyclin-dependent kinases (CDKs) [50,51]. p21 is a protein kinase inhibitor that plays a crucial role in regulating cell cycle progression. By inhibiting CDK4, CDK6, and cyclin D, as well as CDK2 and cyclin E, p21 promotes the temporary arrest of cells at the G1/S and G2/M transitions [52,53]. The results from Fig. 3d demonstrated that A549 cells exposed to 7a, 7b and 7c exhibited a significant reduction in the expression of CDK6, CDK4 and cyclin D1, while the expression of p21 was significantly upregulated, which indicates that the cells were blocked in the G1 phase and unable to progress to the S phase, and resulted in an increase in the proportion of cells in the G0/G1 phase, which was consistent with the findings from the cell cycle analysis.

Autophagy plays a key role in regulating cellular processes, maintaining tissue integrity and determining the course of cellular demise. Promoting autophagy represents a potential avenue for the treatment of tumors. Autophagy is a process that swallows its own cytoplasmic proteins or organelles and encapsulates them into vesicles, where they combine with lysosomes to form autophagic lysosomes that degrade their encapsulated contents. Autophagy plays a key role in maintaining cellular homeostasis [54]. Incidence of autophagy can result in a formation of autophagic particle or autophagic vesicle. To investigate the ability of 7a, 7b and 7c cause autophagy, we used monodansylcadaverine (MDC) as a probe to examine the autophagic effect. As observed from Fig. S6 (SI), after a treatment of A549 cells with 8.5 μM of 7a, 4.5 μM of 7b and 8.9 μM of 7c for 20 h, the autophagic vesicles were discovered in the complexes-treated group in comparison to the control. It is well known that the upregulation of Beclin-1 and downregulation of p62 proteins are a mark of autophagic occurrence. As shown in Fig. 3e, 7a-7c upregulated Beclin-1 and downregulated the expression of p62 protein, which showcases that 7a, 7b and 7c are able to cause autophagy.

2.5. RNA-sequence and signaling pathways

To further explore the mechanism of the complex on the inhibition of tumor cell proliferation and cell death in A549 cells, RNA-seq was performed. Bioinformatics was used to further study and verify the effect of 7b on the gene level of A549 cells. As illustrated in Fig. 4, through the volcano map and the heat map, we can see a significant difference in gene expression between the control and 7b treatment groups. Among them, there were 53 up-regulated genes and 85 down-regulated genes. Then by KEGG enrichment analysis, we found several pathways including p53, TNF and TGF-β signaling pathways. Moreover, GO enrichment analysis discovered differential gene involvement inner mitochondrial membrane protein complex, mitochondrial respirasome, response to oxygen levels, cell population proliferation, regulation of cell migration, ATP biosynthetic process. In summary, RNA-seq results showed that iridium(III) metal complex 7b prevents cell proliferation through p53, TNF and TGF-β signaling pathways, which aligns with the results from cell apoptosis.

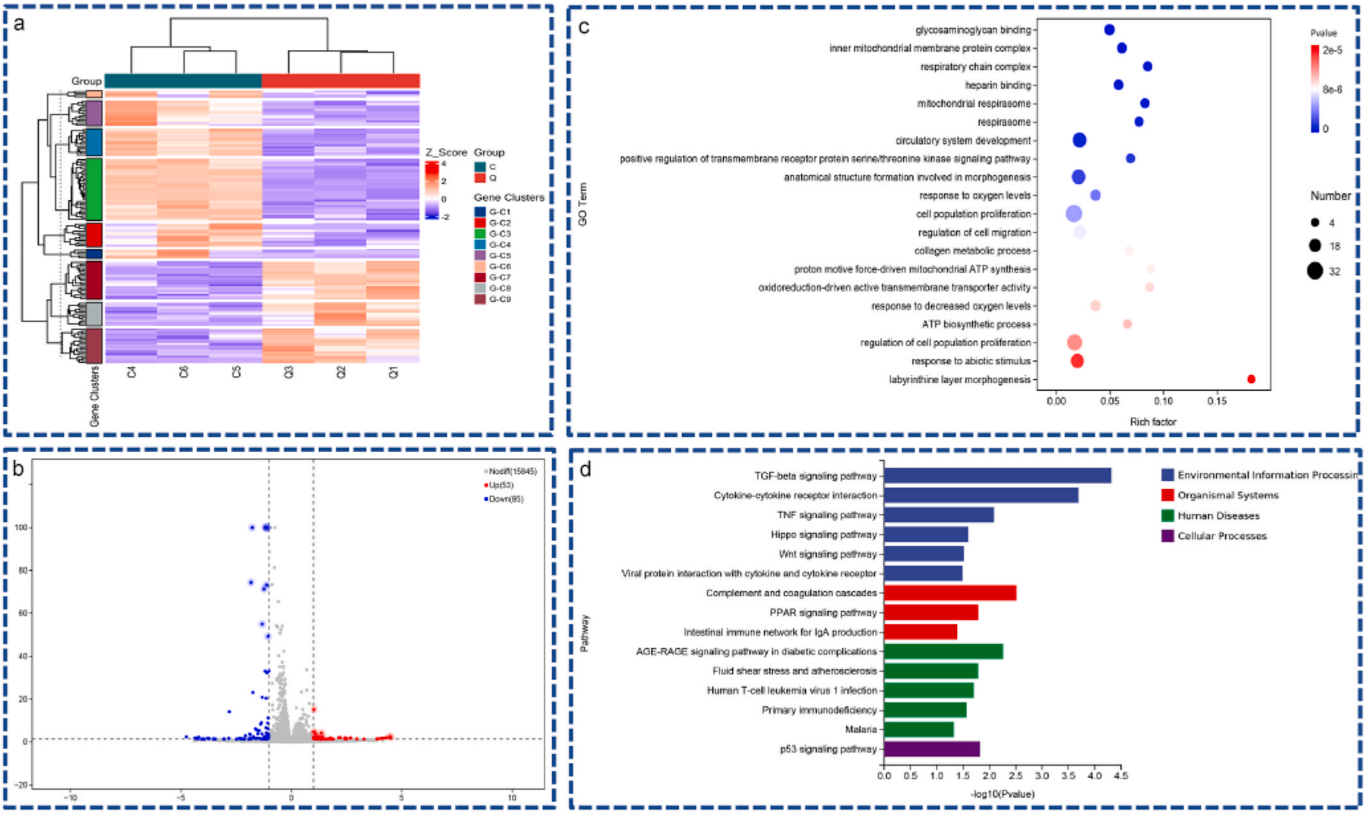

Fig. 4. RNA-sequence analysis in A549 cells exposed to 9.0 μM of 7b for 24 h, (a) heatmap, (b) volcano, (c) GO enrichment, (d) KEGG enrichment.

2.6. *Pyroptosis studies*

Pyroptosis is a type of programmed cell death, one of several forms of programmed cell death. Pyroptosis represents a promising therapeutic target for overcoming tumor drug resistance and triggering anti-tumor immune responses [55,56]. Mitochondrial damage has been demonstrated to enhance the onset of cellular pyroptosis and to amplify downstream inflammatory responses. To investigate the effect of 7a, 7b and 7c on pyroptosis, a morphological examination of cells was conducted. As shown in Fig. 5a, A549 cells were co-incubated with 7a, 7b, and 7c for 20 h, we uncovered the formation of bubbles (red triangles), which is caused because of the disruption of cell membranes and cell swelling, which is driven by the difference in osmotic pressure between the interior of the cell and the external environment of the cell. On the other hand, LDH (lactate dehydrogenase) release is a direct indicator of pyroptosis, when the integrity of the cell membrane is disrupted, LDH is released from the cell, resulting in an increase in the extracellular content of LDH [57]. As illustrated in Fig. 5b, A549 cells were treated with 7a, 7b, or 7c, the LDH content was increased, indicating the rupture of A549 cell membrane. These results suggest that 7a, 7b, and 7c are capable of inducing pyroptosis.

Pyroptosis can be defined as an inflammatory cell death process. The involvement of NF-κB protein is a necessary component, as it has a substantial influence on the inflammatory cascade. The key function of NF-κB proteins is to activate the pro-inflammatory entity caspase 1. The activation of caspase 1 initiates the cleavage of GSDMD-F to GSDMD-N, which results in the perforation of the cell membrane, cellular rupture, and subsequent release of cellular contents. As illustrated in Fig. 5c, the expression of NF-κB protein was found to be elevated, while caspase 1 expression demonstrated a notable reduction, GSDMD-F was transferred into GSDMD-N. Taken together, we consider that 7a, 7b, and 7c can induce pyroptosis.

2.7. *Main death mode studies*

In this article, we found that 7a-7c cause cell death through apoptosis, pyroptosis, autophagy. To validate the main mode to cause cell death, we applied inhibitors Z-VAD-FMK (20 μM), VX765 (0.8 μM) and 3-MA (20 μM) for apoptosis, pyroptosis and autophagy to explore the main manner. In the first, we investigated the change of cell viability. As shown in Fig. 6a, addition of Z-VAD-FMK and VX765 led to an increment in the cell viability of 27.3 % and 19.7 % in comparison to 7c alone, while 3-MA only increased by 2.2 %, indicating that the main manners of causing cell death are apoptosis and pyroptosis. Also, we examined the early and late apoptotic percentage. As depicted in Fig. 6b, the total apoptotic percentage in the early and late decreased by 10.61 %, indicating that apoptosis is main manner to induce cell death. Taken together, it can conclude that apoptosis and pyroptosis are the main mode to trigger cell death.

To further affirm the above results, we explored the expression of caspase 1 for pyroptosis, p62 for autophagy, caspase 3 for apoptosis. As illustrated in Fig. 6c–e, the downregulation of caspase 1 and caspase 3 was blocked compared with 7c alone. These results further demonstrate that the cell death is mainly caused by apoptosis and pyroptosis.

2.8. *Acute toxicity and antitumor in vivo*

The maximum tolerated dose (MTD) of an antineoplastic drug in vivo can be initially assessed by observing the behavior and body weight changes of the animals after administration. The in vitro experiments indicated that 7b exhibited the highest anticancer activity among these complexes, therefore, it was selected for further investigation in vivo. Healthy Kunming mice were randomly assigned to four groups: control, 12.5 mg/kg, 25 mg/kg and 50 mg/kg of 7b, each received a continuous administration of 7b over a 10-day period. Fig. 7a illustrates the weight change of mice. The weight change trend in the 12.5 mg/kg administration group and the control group mice is comparable, exhibiting a slow growth pattern. The weight of mice in the 25 mg/kg administration group exhibited a slight decline from the 2nd to 5th day, followed by a gradual increase from the 6th day onwards. In contrast, the body weight of mice in the 50 mg/kg dosing group exhibited a sharp decline during the initial seven days of dosing, followed by a period of relatively stable weight. On the 9th day of this period, one mouse in this group died. Furthermore, an examination of the behavior and hair status of mice in each group throughout the experiment revealed that the hair of mice in both the control group and the 12.5 mg/kg administration group was smooth and neat, and their behavior was active. The mice in the 25 mg/kg administration group exhibited slight messiness in their fur, accompanied by a small amount of fecal contamination. Additionally, their overall behavior was reduced, and they displayed a tendency to curl up in a corner. In the 50 mg/kg dosing group, the hair of the mice exhibited a messy and dull appearance, and secretions adhered to the mouth, nose, and vagina. Furthermore, the mice displayed aberrant behavior, including a reduction in overall activity and a tendency to lie in a prone position. The results indicate that the LD_{50} value of 7b against healthy Kunming mice is 25 mg/kg.

The LD50 value, as determined by the 10-day acute toxicity test, is 25 mg/kg for 7b. In the antitumor in vivo assay, we selected about 1/14LD_{50} and 1/9LD_{50} values as dosing groups. A xenogeneic A549 lung cancer model was constructed in BALB/c nude mice. The mice were randomly divided into three groups: control group, low dosing group (1.8 mg/kg), and high dosing group (2.7 mg/kg). We administered an intraperitoneal injection of 7b into nude mice for seven consecutive days. During this period, we monitored and recorded the mice's daily

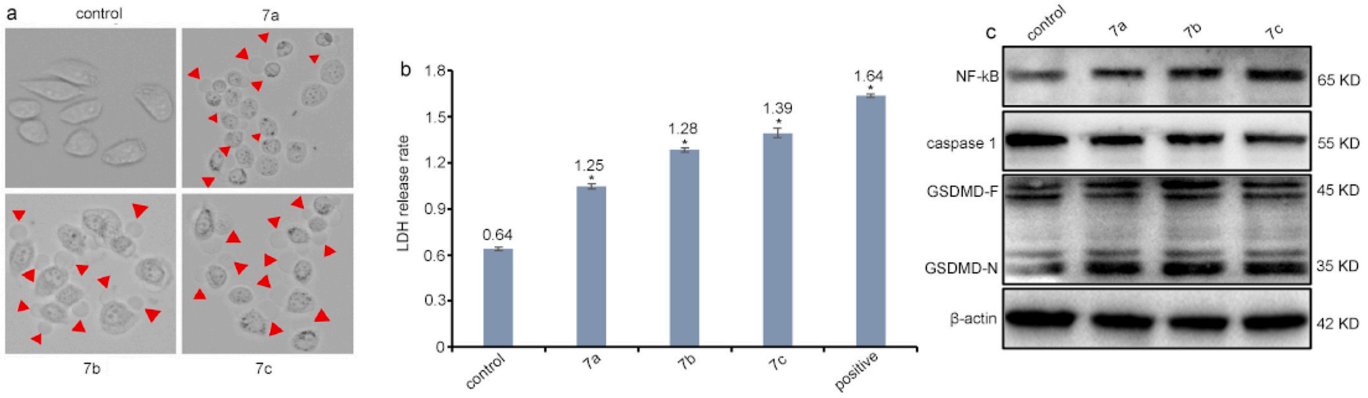

Fig. 5. Pyroptosis assay: (a) cell morphology, (b) LDH release (positive: LDH release reagent), (c) expression of NF-κB, caspase 1 and GSDMD while a 20 h-treatment of A549 cells with IC_{50} concentration of 7a, 7b and 7c.

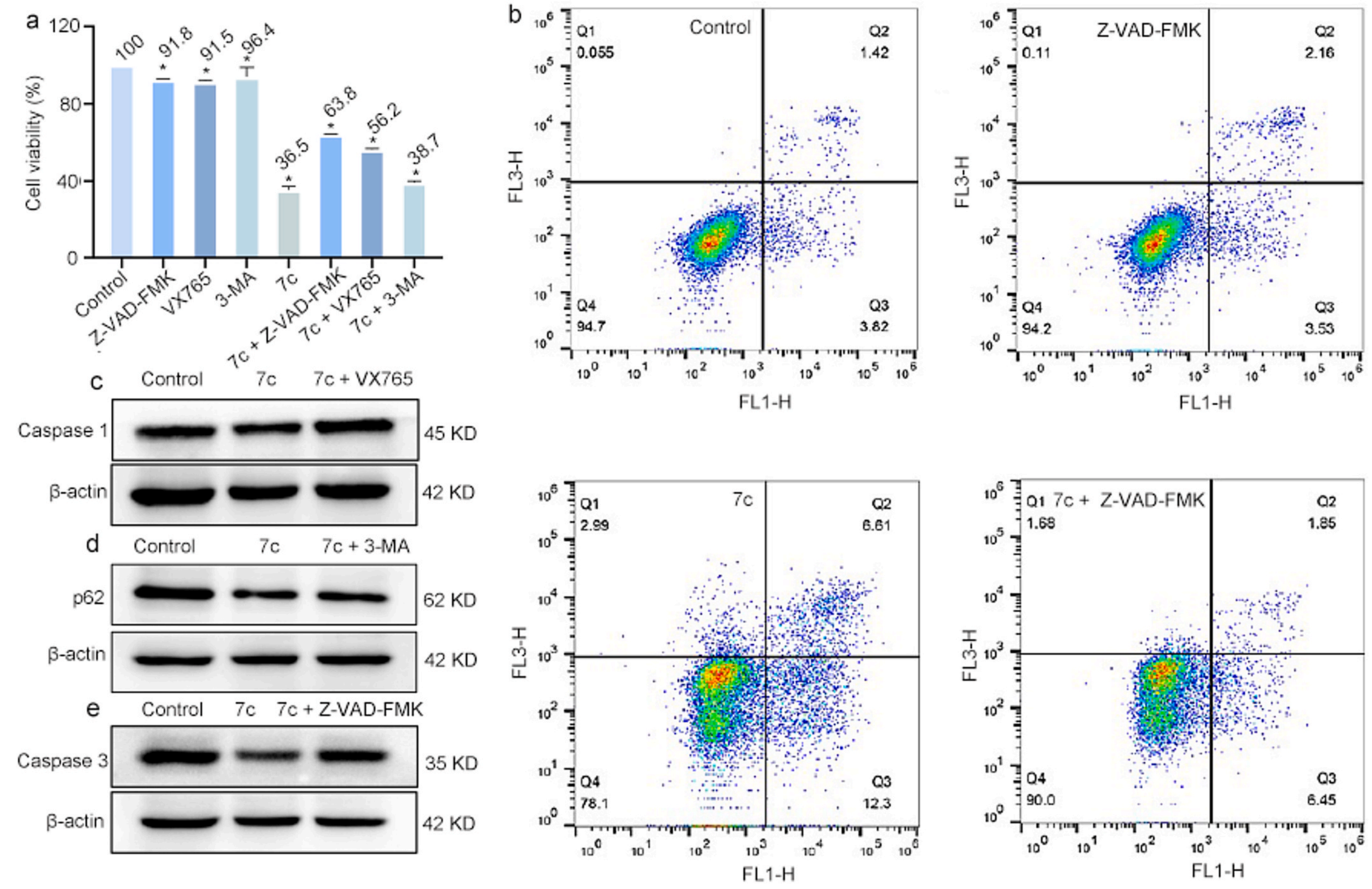

Fig. 6. (a) cell viability assay of A549 cells exposure to IC_{50} concentration of 7c for 36 h, (b) apoptosis assay of A549 cells exposure to IC_{50} concentration of 7c for 12 h, (I) control, (II) Z-VAD-FMK, (III) 7c, (IV) 7c + Z-VAD-FMK, (c–e) expression of caspase 1, p62 and caspase 3 while A549 cells were exposed to IC_{50} concentration of 7c for 24 h.

body weight and tumor size. After 7 days, following the euthanasia of nude mice and the subsequent collection of the tumor and its principal organs. As illustrated in Fig. 7b, the administration group exhibited a significantly inhibited tumor growth compared to the control group. Fig. 7c illustrates that there was no statistically significant difference in body weight between the control and drug-treated groups. Fig. 7d reveals that the relative tumor volume in the control group exhibited a rapid increase. In contrast, the growth trend of the low-dose group was slower than that in the control group. Furthermore, the growth rate in the high-dose group was notably slower and significantly lower than that in the control group and the low-dose group. The mean tumor weight (Fig. 7e) for the three groups was 0.88 g, 0.65 g, and 0.29 g, respectively. The tumor inhibitory rates in the 1.8 mg/kg, 2.7 mg/kg administration group were 26.1 % and 66.9 %. In the Fig. 7f, the weights of heart in the control, 1.8 mg/kg and 2.7 mg/kg are 0.1155 ± 0.02, 0.1009 ± 0.009 and 0.1109 ± 0.008 g, respectively. Therefore, the shape and weight of heart have no obvious change. These findings demonstrated that 7b exhibited high anti-tumor efficacy with no apparent adverse effects on mice.

H&E staining and pathological analysis were performed on key organs and tumor. The results are presented in Fig. 7g. There were no discernible abnormalities in the heart, liver, spleen, lung, and kidney in the administration group compared with the control group. The lung of nude mice treated with 7b exhibited a small number of granulocytes, hemorrhage of bronchioles and peripheral alveoli, and an irregular arrangement of their epithelial cells. The combined experimental data indicated that 7b exhibited anti-tumor activity in vivo and did not result in any significant toxic effects on various organs.

Subsequently, immunohistochemistry (ICH) analysis was conducted on the three groups of tumors, with the markers of DNA damage and cell proliferation-related antigen Ki67 being studied, respectively. As illustrated in Fig. 7h, in the assay of γH2AX, the positive rate in the control, 1.8 mg/kg and 2.7 mg/kg groups are 0.51 %, 2.61 % and 13.70 %. This suggests that the complex can cause apoptosis. While in the assay of Ki67, the positive rates are 18.96 %, 7.52 % and 5.84 % in the control, 1.8 mg/kg and 2.7 mg/kg groups, a decrease of the positive rate indicates that the complex can prevent tumor proliferation. The results indicated that 7b could induce apoptosis and inhibit tumor proliferation. In conclusion, these findings demonstrate the potent anti-tumor efficacy of 7b in vitro and in vivo, as well as its favorable safety profile in key organs. Therefore, it can be proposed that 7b may be a suitable drug candidate for the treatment of non-small cell lung cancer.

2.9. Mechanism studies of inhibiting tumor growth

2.9.1. Immunogenic cell death assay

Immunogenic cell death (ICD) is a form of regulated cell death that activates tumor-specific immune responses in the presence of normal immune function. Tumor cells expose the endoplasmic reticulum proteins calreticulin (CRT) and heat shock proteins (HSP) to the cell membrane during the pre-apoptotic phase, while releasing the nuclear protein high mobility group box-1 (HMGB1) extracellularly, and these signaling factors promote the uptake of dying cells by macrophages [58]. Inducing tumor cells to undergo immunogenic cell death to release damage-associated molecular patterns has become a key component in antitumor therapy [59].

Surface-exposed CRT, HMGB1 and HSP70 were analyzed by smart cell imaging to explore whether 7a, 7b and 7c could induce ICD in A549

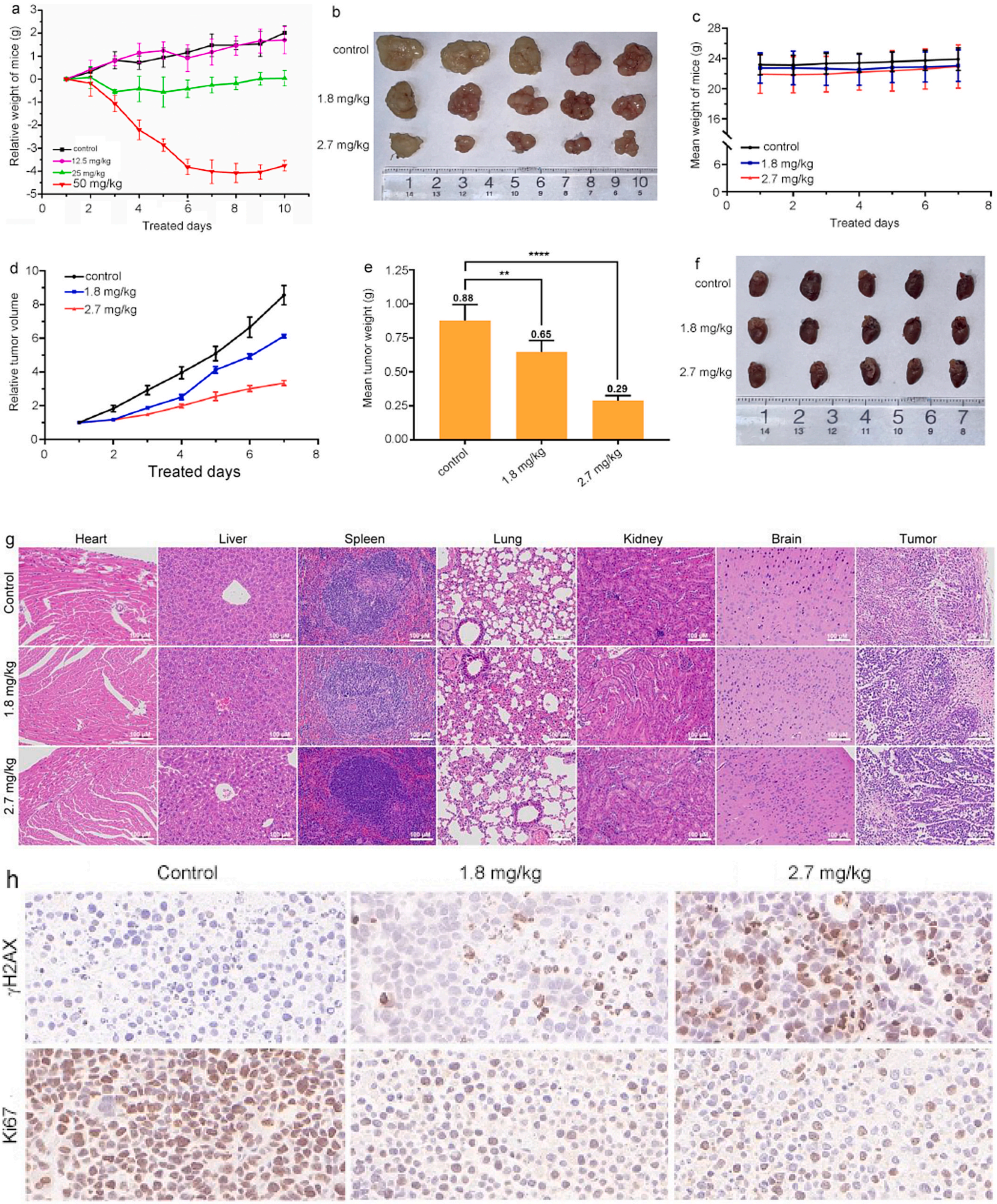

Fig. 7. (a) The relative weight of mice in 10 treated days during the treatment with different concentration of 7b (12.5, 25 and 50 mg/kg), (b) shape of tumor, (c) Mean weight of mice, (d) relative tumor volume, (e) mean weight of tumor, (f) heart of mice, (g) H&E staining assay of heart, liver, spleen, lung, kidney, brain, and tumor, (h) Immunohistochemical analysis of γH2AX and Ki67 in tumor tissues of xenograft nude mice.

cells. As major markers of ICD, the adenosine triphosphate (ATP) secretion, calreticulin (CRT) exposure on the membrane, and high mobility group box 1 (HMGB1) release from nuclei content was examined. As shown in Figs. S7a, b, c and d (SI), A549 cells were exposed to IC_{50} concentration of 7a-7c for 24 h, the ATP content increased, the green fluorescence of CRT, HMGB1 and HSP70 on the surface of the drug group was significantly enhanced compared with the blank group. This suggests that the complexes can elicit the release of the damage-associated molecules CRT, HSP70, and HMGB1 from A549 cells, activate tumor-specific immune responses, and show promise for inducing immunogenic cell death in A549 cells. Meanwhile, we also used Western blot to confirm the upregulation of the expression of CRT, HSP70 and MHGB1 (Fig. S7d and SI), the Western blot results were consistent with the results obtained from the Smart Cell Imager, further confirming that 7a, 7b and 7c may induce immunogenic cell death.

2.9.2. Activation of the immune response

IFN-γ, TNF-α and IL-10, as an important cytokine involved in the immune response, play a key role in combating tumorigenesis and progression. Firstly, LLC (mouse lung cancer) cells were injected into the black C57BL/6J mice, after 7 days, the blood was obtained, the content of cytokines IL-10, IFN-γ and TNF-α was measured using ELISA method. The results shown in Fig. 8a revealed that the content of IL-10 was significantly lower than those of the blank group, while the contents of IFN-γ and TNF-α were higher than those in the control group. The results demonstrated that 7b and 7c could further enhance the antitumor effect by reducing the content of IL-10 and increasing IFN-γ and TNF-α.

GM1, an important component of lipid rafts, is involved in T cell maturation, activation, and the formation of immune synapses. Lipid rafts are microstructural domains in cell membranes enriched with sphingolipids and cholesterol that enrich for signaling molecules and promote T-cell receptor (TCR) activation. The high expression of GM1 in $CD8^+$ T cells and its enrichment in lipid rafts allow it to play an important role in regulating signaling and function of $CD8^+$ T cells [60]. We measured $CD8^+$ T cells and GM1 by immunostaining as shown in the Fig. 8b found that the green fluorescence of the fits 7b and 7c was significantly enhanced compared to the control, indicating an increase in $CD8^+$ T cells. We also determined the percentage of CD44 and CD62L cells in peripheral blood mononuclear cells and spleen by measuring the percentage of CD44 and CD62L cells in peripheral blood mononuclear cells and spleen. It was observed from the Fig. 8c and **d** that compounds 7b and 7c were able to increase the number of CD44 and CD62L cells in

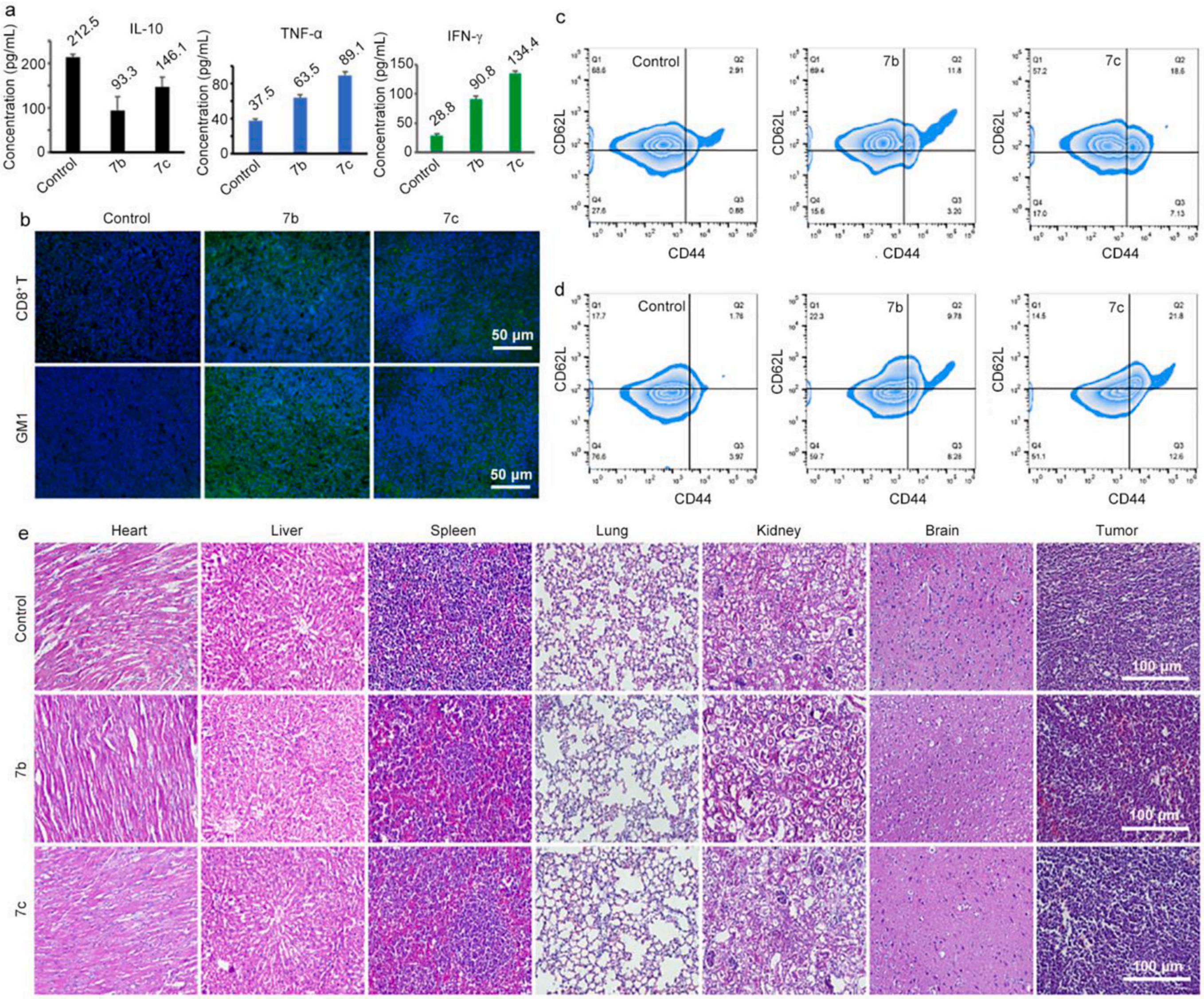

Fig. 8. Determination of lymphocyte from the tumor tissue, (a) the content of TNF-α, IFN-γ and IL-10, (b) GM1 and $CD8^+$ T cells, memory-T cells from the PBMC (c) and spleen (d). (e) H&E staining assay of heart, liver, spleen, lung, kidney, brain, and tumor.

PBMC and spleen.

Tissue organs of mice in each group were stained with H&E to detect pathological damage at the end of the experiment. As shown in Fig. 8e, no significant damage was discovered in the heart, liver, spleen, kidney, and brain in all groups. However, a slight thickening of the alveoli is seen in the lung tissue, and the tumor tissue shows cellular permutation disorganization, nuclear consolidation, and hemorrhage. These suggest that 7b and 7c does not only cause significant damage in mice but also disrupt tumor cell function and cause tumor necrosis.

3. Conclusions

In this study, a new ligand, IPMP, and three new compounds, [Ir(ppy)$_2$(IPMP)]PF$_6$ (7a), [Ir(bzq)$_2$(IPMP)]PF$_6$ (7b), and [Ir(piq)$_2$(IPMP)]PF$_6$ (7c), were synthesized and characterized. The experimental results indicated that the three complexes exhibited the most pronounced inhibitory effect on the proliferation of the A549 cell line. In vitro results have demonstrated that complexes can target the mitochondria, disrupt mitochondrial function, and thereby cause a reduction of mitochondrial membrane potential. These complexes exhibit remarkable efficacy in the inhibition of tumor cell proliferation and migration, as well as in the inhibition of tumor cell growth at the G0/G1 phase. Additionally, the complexes can cause apoptosis, autophagy and pyroptosis, while apoptosis and pyroptosis are two main manners to trigger cell demise. Interestingly, 7b shows high antitumor efficiency with an inhibitory rate of 66.9 %. The mechanism studies illustrate that the complexes induce immunogenic cell death to activate immune response to increase CD8$^+$ T cell and increase the content of cytokines IFN-γ and TNF-α, reduce the content IL-10, which further kill tumor cells. The findings from in vitro experiments demonstrate that the complexes elicit cell death in A549 cells through four distinct pathways (I) The complexes cause a mitochondrial dysfunction, release cyto c, and activate caspase 3, regulate the expression of Bcl-2 family proteins and inducing apoptosis; (II) the complexes cause damage to cellular DNA and microtubules, and block cellular division at the G0/G1 phase, thereby promoting apoptosis; (III) the complexes induce autophagy via inhibiting PI3K/AKT/mTOR signaling pathway; (IV) the complexes regulate NF-κB proteins, thereby activate caspase 1, which induces cellular pyroptosis. Consequently, this work will prove beneficial to the future development of anti-tumor mechanisms and the design of new Ir(III) complexes.

4. Experimental

4.1. Synthesis and characterization

4.1.1. Synthesis of ligand IPMP

To a solution of 1,10-phenanthroline-5,6-dione (2 mmol, 0.42 g) and 2-hydroxyl-4-methylbenzaldehyde (2 mmol, 0.28 g) in glacial acetic acid (30 mL) was added ammonium acetate (40 mmol, 3.1 g) in a three-neck flask. The mixture was stirred at 130 °C and refluxed for 2 h. After cooling the reaction to room temperature, the solution was neutralized with concentrated ammonia water, and the resulting precipitate was washed with double-distilled water. The yellow precipitate was collected by suction filtration, and the IPMP ligand was obtained after drying in a vacuum drying oven. The yield was 89 %. The molecular formula of IPMP is $C_{20}H_{14}N_4O$. ^{1}H NMR (DMSO-d_6, 500 MHz): The signals of the protons in the hydroxyl group (-OH) and in the imidazole ring were not found. δ 9.01 (d, 2H, $J = 7.5$ Hz), 8.85 (d, 2H, $J = 7.5$ Hz), 8.00 (d, 1H, $J = 8.0$ Hz), 7.81–7.79 (m, 2H), 6.86 (d, 2H, $J = 7.5$ Hz), 2.33 (s, 3H). ^{13}C NMR (DMSO-d_6, 125 MHz): 173.01, 167.29, 157.43, 150.67, 149.49, 148.87, 144.41, 139.20, 132.86, 131.66, 130.78, 125.46, 124.23, 122.99, 120.37, 21.60. HRMS (CH_3OH): Calcd for $C_{20}H_{14}N_4O$: $m/z = 326.1168$, Found: $m/z = 325.1049$ ([M − H]$^-$).

4.1.2. Synthesis of 7a, 7b, and 7c

Under argon, IPMP (0.16 g, 0.5 mmol) and *cis*-[Ir(ppy)$_2$Cl]$_2$ (0.27 g, 0.25 mmol) [61] for 7a, *cis*-[Ir(bzq)$_2$Cl]$_2$ (0.30 g, 0.25 mmol) [61] for 7b, *cis*-[Ir(piq)$_2$Cl]$_2$ (0.32 g, 0.25 mmol) [61] for 7c were dissolved in 45 mL CH_3OH/CH_2Cl_2 ($CH_3OH:CH_2Cl_2 = 1:2$, v/v) and refluxed at 40 °C for 6 h. Once the solution has reached room temperature, the excess NH_4PF_6 aqueous solution was added into the solution and stirred for 1.5 h. The solvent was removed through vacuum decompression, resulting in the formation of a yellow powder. The obtained crude product was separated by neutral alumina column chromatography, dichloromethane-acetonitrile (v/v, 4:1) was used as the eluent. The orange-yellow band fractions were collected, concentrated, and dried. Finally, the yellow powder (7a), orange-red powder (7b), and dark red powder (7c) were obtained.

7a: 84 % yield. HRMS (CH_3CN, Fig. S8 and SI): Calcd for $C_{42}H_{30}IrN_6OPF_6$: $m/z = 827.2110$ ([M − PF$_6$]$^+$), found $m/z = 827.2120$ ([M − PF$_6$]$^+$). ^{1}H NMR (DMSO-d_6, 500 MHz, Fig. S9 and SI): The signals of the proton of hydroxyl group in the benzene ring and the proton in the imidazole ring were not observed. δ 9.26 (d, 2H, $J = 8.5$ Hz), 8.26 (d, 2H, $J = 8.0$ Hz), 8.16–8.13 (m, 3H), 8.09–8.06 (m, 2H), 7.95 (d, 2H, $J = 7.5$ Hz), 7.87 (t, 2H, $J = 7.5$ Hz), 7.50 (d, 2H, $J = 6.0$ Hz), 7.06 (t, 2H, $J = 7.5$ Hz), 7.00–6.92 (m, 6H), 6.29 (d, 2H, $J = 7.5$ Hz), 2.35 (s, 3H). ^{13}C NMR (125 MHz, DMSO-d_6, Fig. S10 and SI) δ 172.33, 167.38, 157.66, 150.85, 149.66, 148.93, 144.57, 144.52, 142.79, 139.18, 132.98, 131.71, 130.75, 127.53, 127.17, 125.56, 124.33, 122.86, 120.98, 120.46, 118.05, 21.66.

7b: 86 % yield. HRMS (CH_3CN, Fig. S11 and SI): Calcd. for $C_{46}H_{30}IrN_6OPF_6$: $m/z = 875.2110$ ([M − PF$_6$]$^+$), found $m/z = 875.2120$ ([M − PF$_6$]$^+$). ^{1}H NMR (DMSO-d_6, 500 MHz, Fig. S12 and SI): The signals of the proton of hydroxyl group in the benzene ring and the proton in the imidazole ring were not observed. δ 9.02 (d, 2H, $J = 8.5$ Hz), 8.50 (d, 2H, $J = 8.0$ Hz), 8.18 (d, 1H, $J = 8.0$ Hz), 7.99–7.94 (m, 6H), 7.87 (d, 2H, $J = 8.5$ Hz), 7.82–7.79 (m, 2H), 7.57 (d, 2H, $J = 8.0$ Hz), 7.44 (q, 2H), 7.22 (t, 2H, $J = 7.5$ Hz), 6.77–6.73 (m, 2H), 6.33 (d, 2H, $J = 7.5$ Hz), 2.30 (s, 3H). ^{13}C NMR (DMSO-d_6, 125 MHz, Fig. S13 and SI): 172.48, 157.93, 157.05, 148.99, 148.52, 146.91, 143.53, 140.92, 137.86, 134.19, 132.15, 130.16, 129.94, 127.13, 126.92, 126.26, 124.65, 123.21, 120.61, 119.81, 117.21, 21.53.

7c: 81 % yield. HRMS (CH_3CN, Fig. S14 and SI): Calcd. for $C_{50}H_{34}IrN_6OPF_6$: $m/z = 927.2523$ ([M − PF$_6$]$^+$), found $m/z = 927.2556$ ([M − PF$_6$]$^+$). ^{1}H NMR (DMSO-d_6, 400 MHz, Fig. S15 and SI): The signals of the proton of hydroxyl group in the benzene ring and the proton in the imidazole ring were not observed. δ 9.11 (q, 2H), 9.02 (d, 2H, $J = 8.0$ Hz), 8.40 (d, 2H, $J = 8.0$ Hz), 8.20 (d, 1H, $J = 7.6$ Hz), 8.00 (d, 2H, $J = 9.0$ Hz), 7.94–7.84 (m, 8H), 7.44 (d, 2H, $J = 6.4$ Hz), 7.38 (d, 2H, $J = 6.8$ Hz), 7.16 (t, 2H, $J = 8.0$ Hz), 6.96 (t, 2H, $J = 7.6$ Hz), 6.81–6.78 (m, 2H), 6.32 (d, 2H, $J = 7.2$ Hz), 2.31 (s, 3H). ^{13}C NMR (DMSO-d_6, 125 MHz, Fig. S16 and SI): 172.50, 168.38, 157.88, 154.93, 145.85, 143.39, 141.07, 136.92, 132.45, 132.20, 131.07, 130.97, 129.81, 128.16, 126.99, 126.91, 126.63, 126.04, 125.65, 122.68, 122.64, 120.15, 117.46, 21.62.

4.2. In vitro cytotoxicity test

The cytotoxicity in vitro of 7a, 7b and 7c on the selected cancer cells was tested by 3-(4,5-dimethylthiazole)-2,5-diphenyltetraazolium bromide (MTT) method [28]. The cancer cells were seeded in 96-well plates at a density of 1.0×10^5 cells per well and cultured for 24 h. The different concentration of 7a, 7b and 7c were added into the wells to treat the cancer cells for 48 h, followed by adding 10 μL of MTT and 90 μL of medium. The plate was then incubated in an incubator at 37 °C for 4 h. After incubation, discarding the culture medium, adding 100 μL of DMSO into the plate and shake for 6 min using a multimode microplate reader to determine the absorbance (490 nm). The test was repeated three times independently and the mean value was calculated.

4.3. *Western blotting experiments*

The Western blot was carried out by the following six procedures: (I) A549 cells were seeded evenly in 6-well plates and incubated overnight, when the adherent cells grow to 80 %, the cells were together incubated with IC_{50} concentration of 7a, 7b and 7c at 37 °C for 20 h. (II) After incubation, wash the cells three times with ice-cold PBS, then add the cell lysates to the 6-well plate, scrape the cells in the 6-well plate and place a 1.5 mL tube, and continue lysis for 10 min. At the end of the lysis, the cells are placed in a cryogenic centrifuge and the supernatant is taken as the target total protein. (III) The total protein content was measured using the BCA Quantification Kit and electrophoresed on an SDS-SPAGE gel for 3 h to separate the same amount of denatured protein. A pre-stained colored protein marker was used as an internal reference. (IV) The gel is then split, transferred to a polyvinylidene fluoride membrane, and blocked with 5 % nonfat dry milk in TBST buffer solution for 2 h. (IV) The membrane is hybridized with primary antibody (1:5000 dilution) overnight at 4 °C. (V) Then the membrane is further hybridized with horseradish peroxidase-conjugated secondary antibody (1:5000 dilution) for 2 h. (VI) Each protein was visualized using an enhanced chemiluminescence (ECL) assay kit according to the manufacturer's instructions. Finally, the protein bands were visualized and analyzed in a FluorChem E instrument.

4.4. *Acute toxicity test*

Healthy mice from the Guangdong Medical Laboratory Animal Center (Guangzhou, China) were randomly divided into four groups. Each group consisted of half male and half female mice, and the mice were fed in the Animal Experiment Center of Guangdong Pharmaceutical University. The mice were housed in a temperature-controlled environment (25 °C) with a relative humidity of 40–50 %. The feeding conditions and experimental methods were conducted in accordance with the relevant regulations and principles of the Animal Center of Guangdong Pharmaceutical University and approved by the Animal Ethics Committee of Guangdong Pharmaceutical University. Following the safety quarantine period, the four groups of mice were designated as the blank control group and the experimental group (7b at concentrations of 0, 12.5, 25, and 50 mg/kg, respectively). The body weight of each mouse was recorded at the same time each day, and 7b of each concentration gradient was injected intraperitoneally. The mouse hair and its activity status were monitored and recorded. Following a 10-day period of continuous administration, the mice were injected with 150 mg/kg sodium isoambarbital and subsequently euthanized via cervical dislocation following anesthesia. The maximum tolerated dose of mice was ultimately determined based on the drug concentration, weight, hair, and behavioral characteristics of the mice.

4.5. *In vivo antitumor activity*

Given the evident in vitro toxicity of 7b on A549 cells, the in vivo anti-tumor effect of 7b was investigated using the A549 xenograft tumor model. The BALB/c nude mice were obtained from the Guangdong Medical Laboratory Animal Center (Guangzhou, China) and were maintained in the Animal Experiment Center of Guangdong Pharmaceutical University (25 °C, relative humidity 40–50 %) in a specific pathogen-free (SPF) environment. All experimental procedures were approved by the Animal Ethics Committee of Guangdong Pharmaceutical University. A549 cells exhibiting robust growth characteristics were directly inoculated beneath the armpits of nude mice. Following a seven-day incubation period, small cauliflower-like tumors emerged at the site of tumor inoculation in the mice. The mice were randomly divided into three groups, with six mice in each group and half male and half female, respectively. The groups were designated as the blank control group, the low dose group (1.8 mg/kg), and the high dose group (2.7 mg/kg). Once the tumor reaches approximately 5 mm in diameter, the mice are administered with the drug in a seven-dose regimen. The tumor size and mice weight were recorded throughout the experiment. Finally, the tumors were peeled off and the brain, heart, liver, spleen, and lung tissues were collected, and the slices were stained with *hematoxylin*-eosin (H&E).

4.6. *Assay of immunofluorescence staining*

LLC (mouse lung cancer) cells were injected the black C57BL/6J mice, we observed the tumor model after 7 days. Then 2.7 mg/kg 7b was intraperitoneally injected the mice for continuous 7 days. The tumors were excised, then the tumors were taken into the embedding box, dehydrated for 15 h, embedded in paraffin, and gain the tumor sections. The sections were baked overnight, dewaxed according to the procedure, and put into citrate antigen repair solution to repair the sections. After cooling, the sections were closed with a drop of goat serum blocking solution for 1 h, then incubated with primary antibody overnight. Next day, the secondary antibody was incubated for 1 h, then Hoechst 33342 was incubated for 5 min in the dark, and anti-fluorescent bursting agent was added to close the sections. Ultimately, the sections were observed under fluorescence microscope.

4.7. *Data analysis*

Statistical significance was assessed with t-tests and $^*P < 0.05$ is significant.

Note: The experimental procedure for material and methods, cell culture, cellular uptake, cell scratch experiment, cell cloning experiment, mitochondrial damage, mitochondrial localization and mitochondrial membrane potential, apoptosis assay, cell cycle arrest studies, γH2AX detection, α-tubulin assay, cytochrome *c* release, autophagy, lactate dehydrogenase (LDH) release and ATP determination can be discovered in the Supporting Information.

CRediT authorship contribution statement

Shuanghui Tang: Writing – original draft, Methodology, Investigation. **Yueyao Ding:** Investigation, Formal analysis, Data curation. **Ziyan Zhang:** Investigation, Data curation. **Yan Yang:** Writing – original draft, Methodology, Conceptualization. **Chunxia Huang:** Investigation, Formal analysis. **Lin Zhou:** Formal analysis, Data curation. **Shuang Tian:** Software, Formal analysis. **Hui Yin:** Writing – review & editing, Funding acquisition, Conceptualization. **Yunjun Liu:** Supervision, Project administration, Funding acquisition.

Declaration of competing interest

Authors declare no competing interests exist.

Acknowledgements

This research was supported by the National Natural Science Foundation of China (Nos. 21877018, 82171700).

Appendix A. Supplementary data

Supplementary data to this article can be found online at https://doi.org/10.1016/j.ejmech.2025.117926.

Data availability

Data will be made available on request.

References

[1] F. Bray, M. Laversanne, H. Sung, J. Ferlay, R.L. Siegel, I. Soerjomataram, A. Jemal, Global cancer statistics 2022: GLOBOCAN estimates of incidence and mortality worldwide for 36 cancers in 185 countries, CA Cancer J. Clin. 74 (2024) 229–263.

[2] S.Y. Yin, Y. Yu, N. Wu, M. Zhuo, Y.M. Wang, Y.J. Niu, Y.Q. Ni, F. Hu, C.M. Ding, H. S. Liu, X.H. Cheng, J. Peng, J. Li, Y. He, J.X. Li, J.Y. Wang, H.S. Zhang, X.Y. Zhai, B. Liu, Y.Q. Wang, S. Yan, M.L. Chen, W.Q. Li, J.C. Peng, F. Peng, R.B. Xi, B.Q. Ye, L.Y. Jiang, J.J. Xi, Patient-derived tumor-like cell clusters for personalized chemo- and immunotherapies in non-small cell lung cancer, Cell Stem Cell 31 (2024) 717–733.e8.

[3] S. Tukagoshi, Cancer chemotherapy; past, present and future–from the aspect of fundamental studies, Gan To Kagaku Ryoho. 30 (2003) 1398–1403.

[4] M.O. Grimm, F.H. Hartmann, R. Ackermann, Zukunft der Chemotherapie, Urologe 45 (2006) 567–571.

[5] P. Behinaein, J. Treffalls, H. Hutchings, I.C. Okereke, The role of sublobar resection for the surgical treatment of non-small cell lung cancer, Curr. Oncol. 30 (2023) 7019–7030.

[6] M.K. Mayekar, T.G. Bivona, Current landscape of targeted therapy in lung cancer, Clin. Pharmacol. Ther. 102 (2017) 757–764.

[7] R. Rui, L. Zhou, S. He, Cancer immunotherapies: advances and bottlenecks, Front. Immunol. 14 (2023) 1212476.

[8] L.Y. Qi, Q. Luo, Y.Y. Zhang, F.F. Jia, Y. Zhao, F.Y. Wang, Advances in toxicological research of the anticancer drug cisplatin, Chem. Res. Toxicol. 32 (2019) 1469–1486.

[9] Y. Han, P.Y. Wen, J.J. Li, K. Kataoka, Targeted nanomedicine in cisplatin-based cancer therapeutics, J. Contr. Release 345 (2022) 709–720.

[10] Y.I. Yang, J.H. Ahn, Y.S. Choi, J.H. Choi, Brown algae phlorotannins enhance the tumoricidal effect of cisplatin and ameliorate cisplatin nephrotoxicity, Gynecol. Oncol. 136 (2015) 355–364.

[11] S. Ghosh, Cisplatin: the first metal based anticancer drug, Bioorg. Chem. 88 (2019) 102925.

[12] T.F. Yang, M.h. Zhu, M. Jiang, F. Yang, Z.l. Zhang, Current status of iridium-based complexes against lung cance, Front. Pharmacol. 13 (2022) 1025544.

[13] K.V. Sudheesh, P.S. Jayaram, A. Samanta, K.S. Bejoymohandas, R.S. Jayasree, A. Ajayaghosh, A cyclometalated Ir(III) complex as a lysosome-targeted photodynamic therapeutic agent for integrated imaging and therapy in cancer cells, Chemistry 24 (2018) 10999–11007.

[14] S.L. Yi, Z. Lu, J. Zhang, J. Wang, Z.H. Xie, L.X. Hou, Amphiphilic gemini Iridium (III) complex as a mitochondria-targeted theranostic agent for tumor imaging and photodynamic therapy, ACS Appl. Mater. Interfaces 11 (2019) 15276–15289.

[15] X.D. Song, X. Kong, S.F. He, J.X. Chen, J. Sun, B.B. Chen, J.W. Zhao, Z.W. Mao, Cyclometalated iridium(III)-guanidinium complexes as mitochondria-targeted anticancer agents, Eur. J. Med. Chem. 138 (2017) 246–254.

[16] K. Xiong, Y. Chen, C. Ouyang, R.L. Guan, L.N. Ji, H. Chao, Cyclometalated iridium (III) complexes as mitochondria-targeted anticancer agents, Biochimie 125 (2016) 186–194.

[17] M. Ouyang, L.L. Zeng, H.Y. Huang, C.Z. Jin, J.P. Liu, Y. Chen, L.N. Ji, H. Chao, Fluorinated cyclometalated iridium(iii) complexes as mitochondria-targeted theranostic anticancer agents, Dalton Trans. 46 (2017) 6734–6744.

[18] C.X. Huang, Y.H. Yuan, G.C. Li, S. Tian, H.Y. Hu, J. Chen, L.J. Liang, Y. Wang, Y. J. Liu, Mitochondria-targeted iridium(III) complexes encapsulated in liposome induce cell death through ferroptosis and gasdermin-mediated pyroptosis, Eur. J. Med. Chem. 265 (2024) 116112.

[19] X.C. Liu, Z. Wang, X.R. Zhang, X.C. Lv, Y. Song, R.X. Dong, G.X. Li, X.Y. Ren, Z. Y. Ji, X.A. Yuan, Z. Liu, Configurationally regulated half-sandwich iridium(III)-ferrocene heteronuclear metal complexes: potential anticancer agents, J. Inorg. Biochem. 249 (2023) 112393.

[20] Y.H. Yuan, Y.Y. Zhang, J. Chen, C.X. Huang, H.M. Liu, W.L. Li, L.J. Liang, Y. Wang, Y.J. Liu, Synthesis, biological evaluation of novel iridium(III) complexes targeting mitochondria toward melanoma B16 cells, Eur. J. Med. Chem. 247 (2023) 115046.

[21] J. Sanz-Villafruela, C. Bermejo-Casadesus, E. Zafon, M. Martínez-Alonso, G. Durá, A. Heras, I. Soriano-Díaz, A. Giussani, E. Ortí, F. Tebar, G. Espino, A. Massaguer, Insights into the anticancer photodynamic activity of Ir(III) and Ru(II) polypyridyl complexes bearing β-carboline ligands, Eur. J. Med. Chem. 276 (2024) 116618.

[22] I. Echevarra, E. Zafon, S. Barrabés, M.A. Martíne, S. Romas-Gómez, N. Ortega, B. R. Manzano, E.A. Jalón, R. Quesada, G. Espino, A. Massaguer, J. Inorg. Biochem. 231 (2022) 111790.

[23] H.Y. Hu, J. Chen, F. Zhang, Z.J. Sheng, Y. Yang, Y.F. Xie, L. Zhou, Y.J. Liu, Evaluation of efficiency of liposome-entrapped Iridium (III) complexes inhibiting tumor growth in vitro and in vivo, J. Med. Chem. 67 (2024) 16195–16208.

[24] W.J. Li, S.H. Li, M.H. Zhu, G. Xu, X.Y. Man, Z.L. Zhang, H. Liang, F. Yuan, Developing a rhodium(III) complex to reprogram the tumor immune and metabolic microenvironments: overcoming multidrug resistance and metastasis in non-small cell lung cancer, J. Med. Chem. 67 (2024) 17243–17258.

[25] X.Y. Man, W.J. Li, M.H. Zhu, S.H. Li, G. Xu, Z.L. Zhang, H. Liang, F. Yuan, Anticancer tetranuclear Cu(I) complex catalyzes a click reaction to synthesize a chemotherapeutic agent in situ to achieve targeted dual-agent combination therapy for cancer, Angew. Chem. Int. Ed. 63 (2024) e202411846.

[26] G. Xu, Q.Y. Liang, L.J. Guo, S.H. Xu, W.C. Luo, Q.M. Wu, J.Y. Li, Z.L. Zhang, H. Liang, F. Yuan, Developing an arene bi-nuclear ruthenium(II) complex to induce ferroptosis and activate the cGAS-STING pathway: targeted inhibiting growth and metastasis of triple negative breast cancer, J. Med. Chem. 67 (2024) 19573–19585.

[27] T. Meng, Q.P. Qin, Z.L. Chen, H.H. Zou, K. Wang, F.P. Liang, Cyclometalated Ir(III)-8-oxychinolin complexes acting as red-colored probes for specific mitochondrial imaging and anticancer drugs, Eur. J. Med. Chem. 192 (2020) 112192.

[28] P. Szymaszek, M. Tyszka-Czochara, J. Ortyl, Iridium(III) complexes as novel theranostic small molecules for medical diagnostics, precise imaging at a single cell level and targeted anticancer therapy, Eur. J. Med. Chem. 276 (2024) 116648.

[29] S. Tian, H.X. Xu, X.Y. Wu, Y.Y. Ding, L.J. Liang, H. Yin, X.D. Zeng, Y.J. Liu, W. R. Zhu, Ruthenium(II) polypyridyl complexes inhibit tumor growth through stimulating immune system to increase CD8$^+$ T Cell, Eur. J. Med. Chem. 290 (2025) 117470.

[30] W.J. Li, T. Li, Y. Pan, S.H. Li, G. Xu, Z.L. Zhang, H. Liang, F. Yang, Designing a mitochondria-targeted theranostic cyclometalated iridium(III) complex: overcoming cisplatin resistance and inhibiting tumor metastasis through necroptosis and immune response, J. Med. Chem. 67 (2024) 3843–3859.

[31] W.J. Li, S.H. Li, G. Xu, X.Y. Man, T.F. Yang, Z.L. Zhang, H. Liang, F. Yang, Developing a ruthenium(III) complex to trigger Gasdermin E-mediated pyroptosis and an immune response based on decitabine and liposomes: targeting inhibition of gastric tumor growth and metastasis, J. Med. Chem. 66 (2023) 13072–13085.

[32] T. Mosmann, Rapid colorimetric assay for cellular growth and survival: application to proliferation and cytotoxicity assays, J. Immunol. Methods 65 (1983) 55–63.

[33] M.J. Frisch, G.W. Trucks, H.B. Schlegel, G.E. Scuseria, M.A. Robb, J.R. Cheeseman, G. Scalmani, V. Barone, B. Mennucci, G.A. Petersson, H. Nakatsuji, M. Caricato, X. Li, H.P. Hratchian, A.F. Izmaylov, J. Bloino, G. Zheng, J.L. Sonnenberg, M. Hada, M. Ehara, K. Toyota, R. Fukuda, J. Hasegawa, M. Ishida, T. Nakajima, Y. Honda, O. Kitao, H. Nakai, T. Vreven, J.A. Montgomery Jr., J.E. Peralta, F. Ogliaro, M. Bearpark, J.J. Heyd, E. Brothers, K.N. Kudin, V.N. Staroverov, T. Keith, R. Kobayashi, J. Normand, K. Raghavachari, A. Rendell, J.C. Burant, S.S. Iyengar, J. Tomasi, M. Cossi, N. Rega, J.M. Millam, M. Klene, J.E. Knox, J.B. Cross, V. Bakken, C. Adamo, J. Jaramillo, R. Gomperts, R.E. Stratmann, O. Yazyev, A. J. Austin, R. Cammi, C. Pomelli, J.W. Ochterski, R.L. Martin, K. Morokuma, V. G. Zakrzewski, G.A. Voth, P. Salvador, J.J. Dannenberg, S. Dapprich, A.D. Daniels, O. Farkas, J.B. Foresman, J.V. Ortiz, J. Cioslowski, D.J. Fox, Gaussian 09, Revision D.01, Gaussian, Inc., Wallingford CT, 2013.

[34] G.C. Li, J. chen, Y.F. Xie, Y. Yang, Y.J. Niu, X.L. Chen, X.D. Zeng, L. Zhou, Y.J. Liu, White light increases anticancer effectiveness of iridium(III) complexes toward lung cancer A549 cells, J. Inorg. Biochem. 259 (2024) 112652.

[35] J.D. Hood, D.A. Cheresh, Role of integrins in cell invasion and migration, Nat. Rev. Cancer 2 (2002) 91–100.

[36] N.F. Aboubakar, D. Hoton, J. Ambroise, M. Lecocq, M. Vanderputten, Y. Sibille, B. Vanaudenaerde, C. Pilette, C. Bouzin, S. Ocak, Increased expression and activation of FAK in small-cell lung cancer compared to non-small-cell lung cancer, Cancers (Basel) 11 (2019) 1526.

[37] Y.H. Yuan, C.L. Shi, X.Y. Wu, W.L. Li, C.X. Huang, L.J. Liang, J. Chen, Y. Wang, Y. J. Liu, Synthesis and anticancer activity in vitro and in vivo evaluation of iridium (III) complexes on mouse melanoma B16 cells, J. Inorg. Biochem. 232 (2022) 111820.

[38] S.k. Sujan, A. Majumder, P. Sow, A. Samadder, M. Bera, Exploring a new family of designer copper(II) complexes of anthracene-appended polyfunctional organic assembly displaying potential anticancer activity via cytochrome c mediated mitochondrial apoptotic pathway, J. Inorg. Biochem. 243 (2023) 112182.

[39] P. Singh, B. Lim, Targeting apoptosis in cancer, Curr. Oncol. Rep. 24 (2022) 273–284.

[40] S. Ghafouri-Fard, A. Aghabalazade, H. Shoorei, J. Majidpoor, M. Taheri, M. Mokhtari, The impact of lncRNAs and miRNAs on apoptosis in lung cancer, Front. Oncol. 11 (2021) 714795.

[41] S. Islam, W. Qi, C. Morales, L. Cooke, C. Spier, E. Weterings, D. Mahadevan, Disruption of aneuploidy and senescence induced by aurora inhibition promotes intrinsic apoptosis in double hit or double expressor diffuse large B-cell lymphomas, Mol. Cancer Therapeut. 16 (2017) 2083–2093.

[42] Z.C. Zhang, H.N. Yang, G.Y. Wu, Z.Q. Li, T. Song, X.Q. Li, Probing the difference between BH3 groove of Mcl-1 and Bcl-2 protein: implications for dual inhibitors design, Eur. J. Med. Chem. 46 (2011) 3909–3916.

[43] T. Foo, A. George, S. Banerjee, PARP inhibitors in ovarian cancer: an overview of the practice-changing trials, Gene Chromosome Cancer 60 (2021) 385–397.

[44] J.X. Liu, Q. Yuan, X.X. Ling, Q. Tan, H.R. Liang, J.L. Chen, L.Z. Lin, Y.M. Xiao, W. Chen, L.H. Liu, H.W. Tang, PARP-1 may be involved in hydroquinone-induced apoptosis by poly ADP-ribosylation of ZO-2, Mol. Med. Rep. 16 (2017) 8076–8084.

[45] I.E. Hill, M. Boyd, K. Milligan, C.A. Jenkins, A. Sorensen, A. Jirasek, D. Graham, K. Faulds, Understanding radiation response and cell cycle variation in brain tumour cells using Raman spectroscopy, Analyst 148 (2023) 2594–2608.

[46] M. Ando, K. Yoshikawa, Y. Iwase, S. Ishiura, Usefulness of monitoring γ-H2AX and cell cycle arrest in HepG2 cells for estimating genotoxicity using a high-content analysis system, J. Biomol. Screen 19 (2014) 1246–1254.

[47] J.G. Bermudez, A. Deiters, M.C. Good, Patterning microtubule network organization reshapes cell-like compartments, ACS Synth. Biol. 10 (2021) 1338–1350.

[48] M.C. Jones, J. Zha, M.J. Humphries, Connections between the cell cycle, cell adhesion and the cytoskeleton, Philos. Trans. R. Soc. Lond. B Biol. Sci. 374 (2019) 20180227.

[49] P. Binarová, J. Tuszynski, Tubulin: structure, functions and roles in disease, Cells 22 (2019) 1294.

[50] C.Y. Li, Z.J. Liu, G. Wu, Z.Y. Zang, J.Q. Zhang, X.X. Li, J.L. Tao, M. Shen, H.L. Liu, FOXO1 mediates hypoxia-induced G0/G1 arrest in ovarian somatic granulosa cells by activating the TP53INP1-p53-CDKN1A pathway, Development 148 (2021) 199453.

[51] Y.B. Feng, R.W. Niu, X. Cheng, K. Wang, Y. Du, X.Q. Peng, F.H. Chen, ATPR-induced differentiation and G0/G1 phase arrest in acute promyelocytic leukemia by repressing EBP50/NCF1 complex to promote the production of ROS, Toxicol. Appl. Pharmacol. 379 (2019) 114638.

[52] A. Karimian, Y. Ahmadi, B. Yousefi, Multiple functions of p21 in cell cycle, apoptosis and transcriptional regulation after DNA damage, DNA Repair 42 (2016) 63–71.

[53] T. Pai, M.W. Hsu, Y.L. Leu, K.T. Chang, M.S. Weng, Induction of G2/M cell cycle arrest via p38/p21$^{Waf1/Cip1}$-dependent signaling pathway activation by bavachinin in non-small-cell lung cancer cells, Molecules 26 (2021) 5161.

[54] Y.Y. Wu, A.X. Wang, G.T. Feng, X.L. Pan, W. Shuai, P.P. Yang, J. Zhang, L. Ouyang, Y. Luo, G. Wang, Autophagy modulation in cancer therapy: challenges coexist with opportunities, Eur. J. Med. Chem. 276 (2024) 116688.

[55] M.H. Zhang, P.Y. Dang, Y. Liu, B.B. Qiao, Z.Q. Sun, Noncoding RNAs in pyroptosis and cancer progression: effect, mechanism, and clinical application, Front. Immunol. 13 (2022) 982040.

[56] R. Miao, C. Jiang, W.Y. Chang, H.W. Zhang, J. An, F. Ho, P. Chen, H. Zhang, C. Junqueira, D. Amgalan, F.G. Liang, J. Zhang, C.L. Evavold, I. Hafner-Bratkovič, Z. Zhang, P. Fontana, S. Xia, M. Waldeck-Weiermair, Y. Pan, T. Michel, L. Bar-Peled, H. Wu, J.C. Kagan, R.N. Kitsis, P. Zhang, X. Liu, J. Lieberman, Gasdermin D permeabilization of mitochondrial inner and outer membranes accelerates and enhances pyroptosis, Immunity 56 (2023) 2523–2541.

[57] T. Luo, X. Jia, W.D. Feng, J.Y. Wang, F. Xie, L.D. Kong, X.J. Wang, R. Lian, X. Liu, Y.J. Chu, Y. Wang, A.L. Xu, Bergapten inhibits NLRP3 inflammasome activation and pyroptosis via promoting mitophagy, Acta Pharmacol. Sin. 44 (2023) 1867–1878.

[58] A. Ahmed, S.W.G. Tait, Targeting immunogenic cell death in cancer, Mol. Oncol. 14 (2020) 2994–3006.

[59] J. Cui, H.Z. Xu, J. Shi, K. Fang, J. Liu, F. Liu, Y. Chen, H.Y. Liang, Y. Zhang, H. Z. Piao, Carbonic anhydrase IX inhibitor S4 triggers release of DAMPs related to immunogenic cell death in glioma cells via endoplasmic reticulum stress pathway, Cell Commun. Signal. 21 (2023) 167.

[60] V.D.M. Coelho, D. Nguyen, B. Giri, A. Bunbury, E. Schaffer, D.D. Taub, Quantitative differences in lipid raft components between murine CD4$^+$ and CD8$^+$ T cells, BMC Immunol. 5 (2004) 2.

[61] S. Sprouse, K.A. King, P.J. Spellane, R.J. Watts, Photophysical effects of metal-carbon σ bonds in ortho-metalated complexes of iridium(III) and rhodium(III), J. Am. Chem. Soc. 106 (1985) 6647–6653.